Amsterdam University College

Bachelor Thesis

A novel multi-directional light detector for modelling the cost-efficiency benefits of bi-facial solar panels

Student: Andrea Lorenzo Pollastri (AUC, pollastri.andrea815@gmail.com)

Supervisors: dr. Forrest Bradbury (AUC, f.r.bradbury@auc.nl)

dr. Bruno Ehrler (AMOLF, b.ehrler@amolf.nl)

Tutor: dr. ir. Bart Verheggen (AUC, B.Verheggen@auc.nl)

Reader: dr. Marc Davidson

Date: 2nd of June, 2019

Major: Science

Word count: 9598

Five keywords: Solar irradiance, Indirect light, Bi-facial gain, Mono-facial energy yields, LCOE.

AMOLF physics of functional complex matter

Amsterdam University College
Excellence and Diversity in a Global City

Nomenclature

LAD	Light ambiance detector
RE	Renewable energy
BG	Bi-facial energy gain
BFSP	Bi-facial solar panel
MFSP	Mono-facial solar panel
LCOE [USD/kWh]	Levelized cost of electricity
$\pi_{ivt}^{(y)}$ [%]	Percentage of the PV inverter cost for the warranty extension at year y
b [%]	Bifaciality factor
c_{ins} [USD/W_p]	Installation cost of the PV system
$c_{ins,lab}$ [USD/W_p]	Installation cost of the PV system related to the labor
$c_{ins,mat}$ [USD/W_p]	Installation cost of the PV system related to the materials
c_{insu} [%]	Yearly insurance cost factor
$c^{(y)}_{ivt}$ [USD/W_p]	Inverter cost at year y
w_{ivt}[year]	Warranty period of PV inverter
c_{mb} [%]	Cost relation between bi-facial and mono-facial module price to reach the same LCOE
c_{OM} [USD/year/W_p]	Yearly O&M cost factor for PV system
$c_{OM,lab}$ [USD/year/W_p]	Yearly O&M cost factor for PV system related to the labor
$c_{OM,mat}$ [USD/year/W_p]	Yearly O&M cost factor for PV system related to the materials
c_{sp} [USD/W_p]	Acquisition cost of solar panels
$C_{Bank,amor}$ [USD]	Bank amortization payment
$C_{Bank,int}$ [USD]	Bank interest payment
$C_{ini,inv}$ [USD]	PV system initial investment
C_{insu} [USD]	Total insurance cost for PV system
C_{OM} [USD]	Total O&M cost from PV system
C_{own} [USD]	Part of the initial investment paid directly by the project owner
C_{PV} [USD]	Total cost of PV system
$C_{PV,Wp}$ [USD/W_p]	Total system cost per Wp
C_{war} [USD]	Total warranty extension cost of the PV inverter
dt_{Bank} [year]	Bank debt tenor
IR [%]	Inflation rate
IR_{Bank} [%]	Bank interest rate
DR [%]	Discount rate
$E^{(y)}_{PV}$ [Wh]	Total energy generation of the PV system for year y
l_{Bank} [%]	Bank loan
l_S [year]	System lifetime
P_{PV} [W]	Power produced from the PV system
$P_{STC,f}$ [W_P]	Direct power production from the installed solar panels when light reaches only the front side under standard test conditions

Abstract

The increase in CO_2 atmospheric concentrations, global temperatures, and energy demand encourage the decarbonization of the world energy supply sector. With the intention to limit emissions, the 2015 Paris Agreement on climate change concluded with the joint pledge to increase the renewable energy share within the next decade.

The urge to maintain the security of energy supply with less or no fossil fuels requires a high level of maturity and cost-efficiency of sustainable energies. Since the advancement of the first renewable technologies, most of the existing low-carbon energies, especially solar, have experienced a major efficiency development. Furthermore, in the last decades, their cost has decreased in order to render the passage to renewables more feasible. As a consequence of this cost-efficiency improvements, new solar technologies have emerged. In particular, bi-facial solar panels, which are photovoltaic (PV) modules able to detect light from the two opposite faces, have contributed to a significant energy gain.

This project investigates the cost-efficiency benefits of bi-facial solar panels (BFSPs) with respect to their mono-facial counterparts. It confronts the main issues constricting the proliferation of standard mono-facial modules: the high costs and the common efficiency limits below 20%. This thesis concludes an internship at the FOM institute AMOLF that has spanned the academic year. It included the testing and calibration of the twelve sensors of the AMOLF Light Ambiance Detector (LAD) and the analysis of the data it collected in the AMOLF solar field.

The solar irradiance data, obtained by the sky-facing and ground-facing sensors of the LAD, are suitable to the analysis of the energy benefits of a silicon bi-facial solar panel with respect to those of one of the AMOLF mono-facial modules. In this analysis, the ratio of the irradiance values obtained by only the front and back faces of the LAD was preferred, for accuracy reasons, to the data obtained by the twelve faces in the upper and lower hemispheres of the instrument.

For the energy analysis, an 80% bi-faciality factor was considered for the bi-facial panel, while equal energy losses over time were assumed for both solar modules. For the economic analysis, current inverter, fabrication, installation, and maintenance costs were assumed for the total expenditures associated with the solar systems.

The results derived from the LAD's data of the first three months of 2019 reveal that the bi-facial module would exceed the energy yield of the mono-facial panel by a maximum value of about 14%. Furthermore, by considering the mono-facial energy data for a few representative days of 2018, the average bi-facial energy gain over an entire year was estimated at 7.15%. The slightly higher costs connected to a BFSP with respect to a MFSP cause the overall costs, discounted over the lifetime period of a panel, to be 6.7% higher for the former. Finally, considering both generated energies and costs associated to the two modules, the bi-facial LCOE was calculated to be 0.5% lower than the mono-facial LCOE, meaning that BFSPs would be more cost-efficient than MFSPs in the AMOLF solar field. Moreover, by considering predicted future reductions of the fabrication costs of solar inverters and panels and by increasing the surface albedo underneath the panels a lower ΔLCOE could be obtained.

While the results of this thesis are constricted to a bi-facial panel in the AMOLF solar field, the movability of the LAD supports the accessibility of a similar cost-efficiency analysis in other locations.

Acknowledgments

This thesis results from the internship at the FOM institute AMOLF, in Amsterdam, Netherlands, that has spanned the academic year. The project advanced in this paper was made possible by the previous work on the AMOLF light ambiance detector done by the Amsterdam University College student Merlijn Kersten, who I would like to thank for his help and support in the first stages of this research project. Moreover, I would like to express special gratitude to my supervisors dr. Bruno Ehrler and dr. Forrest Bradbury, for their constant guidance to my work. In addition, I would like to thank all the members of the Hybrid Solar Cells Group for welcoming me in their group and helping me get acquainted with the solar instruments and other measurement tools in the AMOLF lab. Furthermore, a special appreciation for their support on my work goes to Moritz Futscher, especially for his help with Mathematica, to ing. Jan Zomerdijk, for his precious assistance during the calibration part of the project and for the supervision of the LAD, to ir. Ivo Klinkert, for developing the software for the LAD's measurements, to ing. Marnix Verwij, for the mechanical work on the LAD and the installation on the instrument in the AMOLF solar field, and to Simon Voogel, for the development of the conversion program for the LAD's data on LINQPad. Finally, I want to thank my reader dr. Marc Davidson for having the time to read this thesis.

Contents

Chapter 1

Introduction

The 2015 Paris climate agreement was based on the joint commitment to maintain the global average temperature below 2 degrees above pre-industrial levels. The countries partaking in the agreement proposed to deliberately contribute to the reduction of carbon dioxide emissions in order to reach the predetermined objective. Most nationally determined contributions for the next decade involved an increase in the renewable energies' (RE) share of the energy supply, due to their low carbon footprint.

While only a mix of RE sources could secure the energy supply, bioenergy, wind, and solar are expected to experience the largest incremental growth, due to their accessibility and level of maturity [5]. In particular, solar energy is expected to spread significantly due to the availability of solar technologies on a market that targets individuals and households as well as organizations.

In 2016, only about 330 TWh [1] were produced through solar panels (SPs), out of the world total energy consumption amounting to almost 151500 TWh [23]. The reason for the solar energy's lack of popularity resides principally in the material and maintenance costs of photovoltaic (PV) modules, in their low efficiency limit[2] [27], and in the intermittent and weather-dependent essence of the power they generate [19]. However, with the ever-increasing demand for energy and the continuous decrease in solar cells' costs, the use of solar energy is destined to increase; a quintupled, with respect to today's value, PV-generated energy amount is indeed expected by 2030 [10].

1.1. Solar energy

Solar energy is the harnessing of the energy the sun emits at a constant rate under the form of electromagnetic radiation. The spectrum of solar radiation resembles that of a black-body with a temperature of 5778 K, which is approximately the temperature of the sun's surface. As shown in Figure 1.1, most (≥ 95%) of the solar radiation corresponds to emission in the visible and infrared ranges of the electromagnetic spectrum.

[1] TWh corresponds to Terawatt-hours. The Tera unit-prefix represents a multiplicative factor of 10^{12}.
[2] The efficiency of a photovoltaic cell (PVC) is determined by the ratio of the electric power output and the total incoming power received through solar irradiation. Even if emerging multijunction cells have reached a 40% limit, commercially available solar modules do not generally exceed an efficiency value of 20% [20].

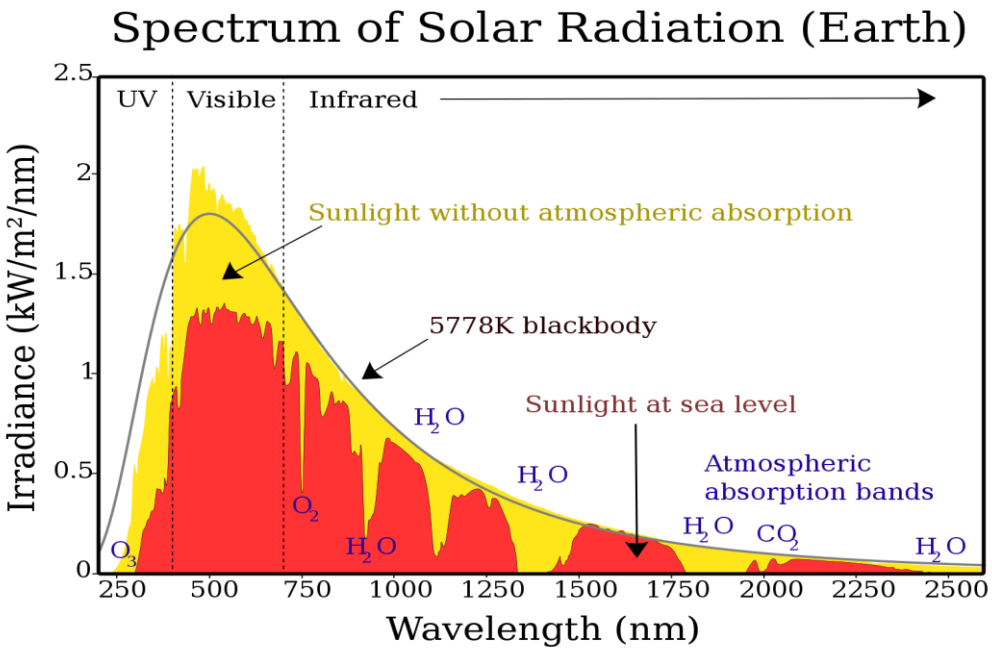

Figure 1.1: The picture illustrates the solar spectrum as measured at the top of the Earth's atmosphere (yellow) and at sea level (red). The solar spectral irradiance resembles that of a black-body with temperature 5778K (black line) [29].

1.2. Silicon solar cells

Photovoltaic cells absorb solar radiation and generate renewable electricity. Since the photovoltaic effect was discovered by Becquerel in 1839 and the first cell with a 1% efficiency was built in 1883, they have experienced a long process of efficiency development [12].

According to their evolution, they are subdivided into three generations. The first generation includes the most popular and commercially available photovoltaic modules: multicrystalline and monocrystalline silicon solar cells.

1.2.1. Silicon's bandgap

The reason for the silicon cells' popularity resides in the electromagnetic properties of silicon and, in particular, in the characteristic bandgap of the semiconductor.

The energy gap (E_g) between the valence and conduction bands of silicon is about 1.12 eV, which corresponds[3] to a wavelength, in the infrared range, of 1107nm[4] [21]. The bandgap represents the minimum energy that a valence-band electron must have in order to be excited to the conduction band. Sunlight photons reaching the valence-band must therefore have an energy higher than the silicon band-gap in order to excite electrons. Hence, a silicon solar cell is able to absorb light with a wavelength lower than 1107nm up until about 400nm, when reflectivity losses start to dominate.

[3] $E = h*v = h*c/\lambda$. Here, "h" corresponds to the Planck constant, "v" to the frequency of the electromagnetic wave, "c" to its speed, and "λ" to its wavelength.
[4] nm = "Nanometers", 10^{-9} m.

1.2.2. Reflectivity losses

The absorption spectrum of silicon cells corresponds to the majority of the solar irradiation's spectrum; thus, such photovoltaic modules are ideal for harvesting sunlight. However, silicon solar cells do not accept all photons, with energy superior to the bandgap, equally. Indeed, according to their wavelengths, photons can be reflected by the silicon surface and by the glass cover on top of it. The reflection coefficient significantly limits the cell's performance at wavelengths lower than 500nm.

1.2.2.1. Silicon

Silicon has a high reflectivity rate due to its high refractive index. Its refractive index is composed of a real part describing the reflectivity of the material and of an imaginary part, which relates to its absorptivity [2]. The absorptivity decreases at low wavelengths since many high energy photons do not get absorbed by the silicon, which has a bandgap much lower than their energy, and pass through it without interacting with the valence-band electrons. Considering the increase of the refractive index (n-ik) at wavelengths lower than 500nm, Figure 1.2 shows the relation between reflectivity losses and photons' wavelength. The observed silicon's surface reflection probability has a minimum value of 30%; while such reflectivity would be deleterious to the transmittance of light through the cell, anti-reflection coatings on top of the bare silicon greatly reduce reflectivity losses in standard solar panels (Figure 1.3).

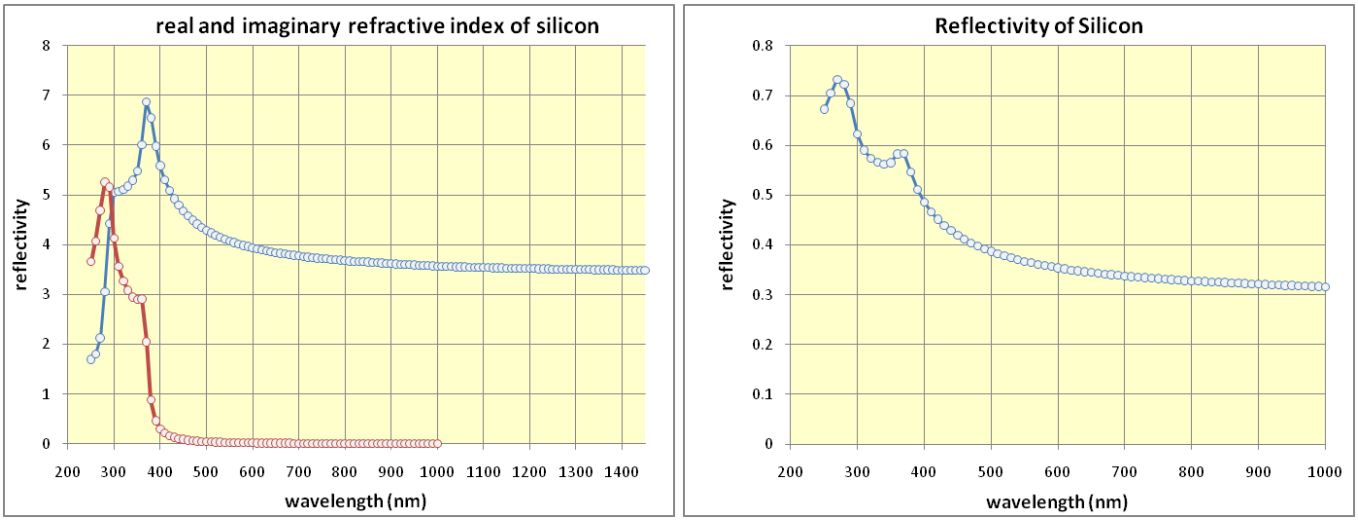

Figure 1.2a,b: a) The line plot (left) shows the real (n, blue) and imaginary (k, red) parts of the refractive index of silicon. b) The graph (right) indicates the reflectivity of the silicon's surface according to photons' wavelength [21].

1.2.2.2. Glass cover

The glass cover on top of a solar panel has a protective purpose against weather adversities and time degradation of the PV cells. The thickness and type of glass are chosen in order to minimize the refractive index at λ=600nm, which corresponds to the wavelength peak of solar radiation (Figure 1.1)

[21]. Figure 1.3 shows the reflection probability for a silicon cell with and without anti-reflection coatings underneath the glass cover. The absorption spectrum is maximum for visible and infrared light.

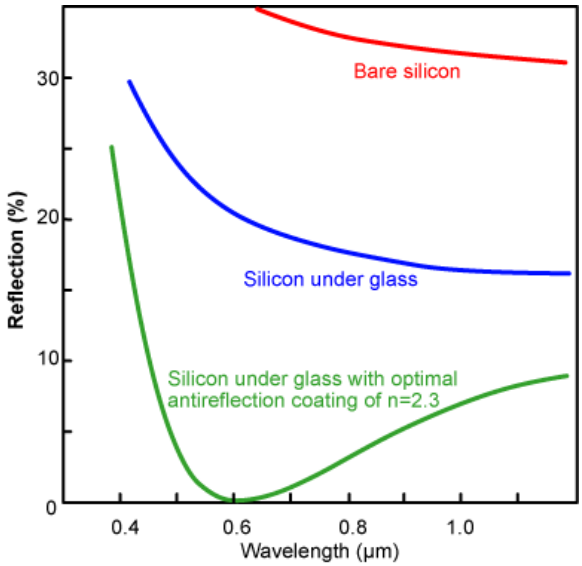

Figure 1.3: The line plots represent the reflection probability of silicon cells with (green) and without (blue) protective coating as compared to pure silicon (red) (section 1.2.2.1) for wavelengths from 300nm to 1200nm [21].

1.2.3. Energy generation

The excited electrons reaching the semiconductor's conduction band leave a hole[5] in the valence band, therefore causing the prevalence of positively charged quasi-particles in the valence band and of negatively charged particles in the conduction band. The electrons and holes diffuse towards the negatively doped (n-type) and positively doped (p-type) sides of the silicon wafer, respectively. The electric potential difference between the two sides induces a current into an external circuit, which is ultimately connected to an inverter. The inverter converts the PV generated direct current into alternating current, which is what we call "electricity", powering any building and appliance.

1.3. Indirect irradiation

[5] The formation of an electron-hole pair (e^-/+) within the bands of the semiconductor generates an electric field inside the PV module (right) [21].

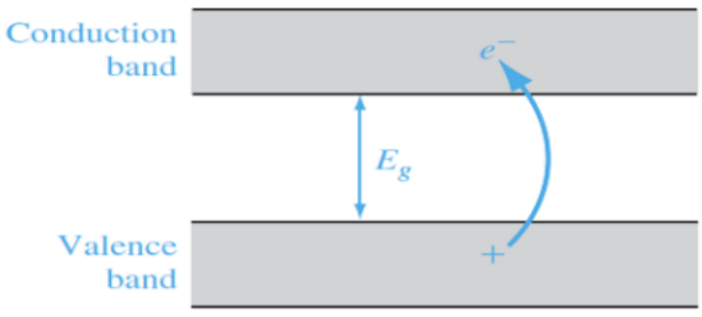

In clear-sky conditions, nearly all incoming light follows the shortest path between the Earth and the Sun. Since the angular aperture subtended by our star, as seen from a point on Earth, is about 0.26° [18], the path is assumed to be a straight line and the light "direct".

Sunlight does not, however, uniquely reach a point on Earth following the shortest path. Although the majority of sunlight is perceived as directly coming from our star, about 15% of the global solar irradiance, on average, comes from diffuse and reflected light, and a higher percentage is received in high latitude regions, in high-albedo and cloudy conditions [18].

Reflected light is, by definition, light that bounces off a surface; it depends on the natural and artificial environment in the proximity of a measurement device and, specifically, on its albedo. The albedo value of a specific surface is the ratio between the radiation[6] it reflects and the solar radiation it receives.

Diffuse irradiation occurs when photons get scattered in multiple directions by particles in the atmosphere, of natural or artificial origin.

1.3.1. Diffuse irradiation

Diffuseness is particularly relevant in cloudy conditions or in areas with high air pollution when sunlight gets scattered in many directions by aerosols. Diffuse light has a much larger angular aperture with respect to direct light and photons can get scattered multiple times before being detected. The randomness and high rate of interactions of photons with particles in the atmosphere decreases the number of photons reaching the Earth's surface, thus decreasing the value of solar irradiance (Figures 2.5b and 2.6b).

Weather conditions of high light diffusivity are typical in the Netherlands, where a portion larger than the global average incoming radiation is diffuse. Between 1961 and 1980, the average diffuse percentage was indeed estimated at 58% [14].

1.4. PV optical losses

Photovoltaic cells do not absorb incoming light equally from all directions: the angle of incidence determines the reflection and transmittance probabilities.

According to Snell's law of refraction[7], the incident angle of the incoming wave and the material's index of refraction determine the angle of refraction inside it. The reflection and transmittance probabilities depend on the angles and refractive indices as well as on the polarization[8] of the wave.

[6] The radiation integrated over the whole solar spectrum.

[7] $n_1*\sin(\theta_i) = n_2*\sin(\theta_i)$ [9].Here, "n_1" and "n_2" are the initial and the material's indices of refraction, respectively. "θ_i" and "θ_r" are the incident and refracted angles, respectively.

[8] Transverse waves, such as light, oscillate perpendicularly to the direction of movement. Polarization is a property of such waves that indicates the orientation of oscillations. In case of electromagnetic (EM) waves, the electric and magnetic field components oscillate perpendicularly to the wave propagation, thus defining two main types of polarization, according to the horizontal or vertical orientation of the electric field with respect to a fixed plane. Many EM waves however result from the

Solar radiation is unpolarized because of the multi-directionality of the oscillations of the photons' components perpendicularly to the propagation. While direct light is assumed to only slightly interact with atoms in the atmosphere, diffuse light is, by definition, scattered by them and polarized in a certain direction. The multiple interactions with aerosols increase the randomness of oscillations; diffuse light is also then assumed unpolarized[9].

Reflection (R) and transmittance (T) probabilities for unpolarized waves are defined as [9]:

$$R = (r_{\perp}^2 + r_{\parallel}^2)/2 \qquad T = 1 - R \qquad (1.1)$$

where "$r_{\perp}$" and "$r_{\parallel}$" indicate the reflection coefficients, derived from Fresnel's equations, of the two types of polarization [9]:

$$r_{\perp} = \frac{n_i \cos(\theta_i) - n_t \cos(\theta_t)}{n_i \cos(\theta_i) + n_t \cos(\theta_t)} \qquad r_{\parallel} = \frac{n_i \cos(\theta_t) - n_t \cos(\theta_i)}{n_i \cos(\theta_t) + n_t \cos(\theta_i)} \qquad (1.2)$$

where indices "i" and "t" indicate the media in which the wave is incident and transmitted, respectively.

Reflection and transmittance probabilities for a silicon solar cell are approximately[10] given by R and T of the system silicon-glass cover, as shown in the code available at https://drive.google.com/file/d/1ZOWB06oVlbu9j_EIDgg-8X428OYbtOqP/view?usp=sharing. Figure 1.4 and 1.5 show, respectively, the reflectivity losses at the glass surface and the transmission probability of sunlight into a silicon cell according to four different wavelengths. The air, glass, and silicon refractive indices depend on wavelength differently. The Cauchy's dispersion equation is used for air and glass for visible light[11], while, for the infrared range, n is assumed constant and equal to that for red light, since the discrepancy from the value corresponding to red is minimum. Silicon has a complex refractive index, but this section neglects its imaginary part, since it is negligible, as compared to the real part, for wavelengths larger than 380nm [15,21].

As expected from Section 1.2.2., the transmission is highest for infrared light and lowest for blue light. Moreover, reflection losses in a solar module grow at high incident angles with respect to the cell's normal vector.

oscillation of the EM components in all directions perpendicular to the wave propagation and are known as unpolarized waves [9]).

[9] Polarization due to reflection at the surface of a material is not considered throughout this paper.

[10] The anti-reflection coating significantly increases the transmittance probability of the silicon cell as compared to Figures 1.4 and 1.5.

[11] Cauchy's equation of $n(\lambda)$ for transparent materials: $n = A + B/\lambda^2$ [11]). "A" and "B" are constants that can be determined if two n's corresponding to two λ's are given. The given λ's for glass and air are derived from [13]. The formula is valid only for λ's in the visible range.

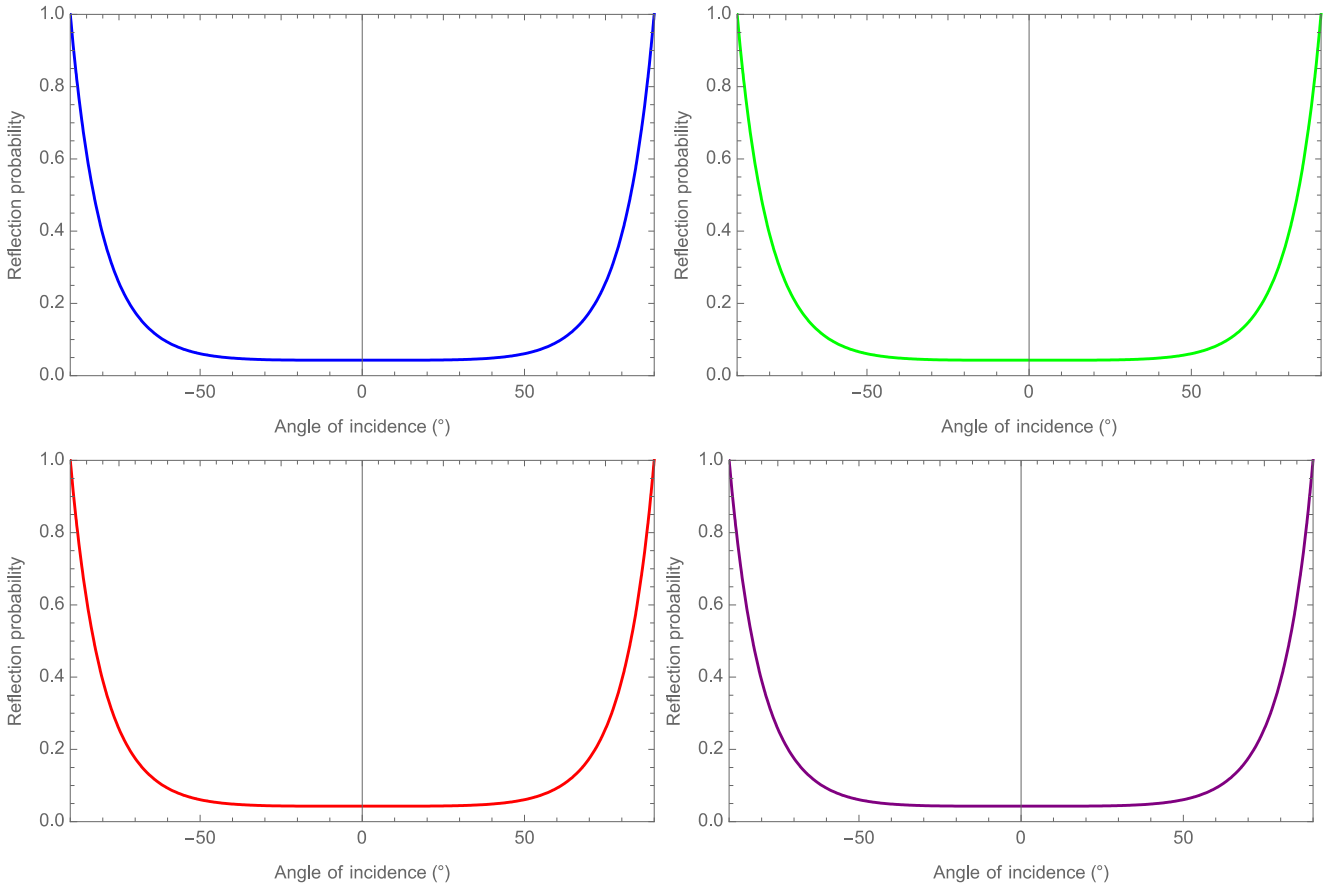

Figure 1.4a,b,c,d: The plots show the reflectivity losses, at the glass surface of a PV system, of incoming photons with a certain wavelength according to their incident angle: a) λ=480nm (Blue); b) λ=520nm (Green); c) λ=620nm (Red); d) λ=820nm (Purple). The previous wavelengths were chosen according to the responsivity peak of the diodes of the LAD [1]. The PV cell is assumed without an antireflection coating.

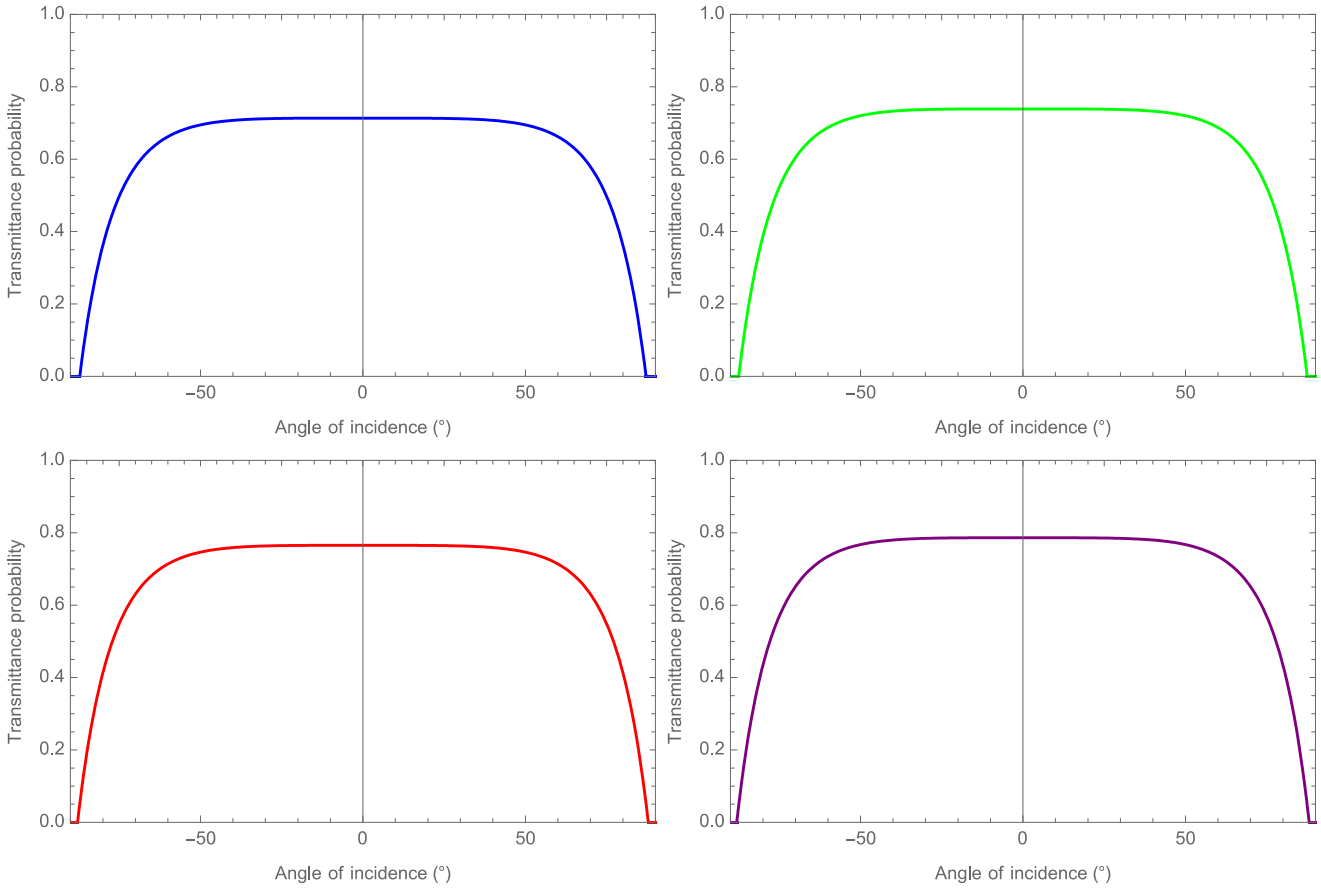

Figure 1.5a,b,c,d: The plots show the transmission probabilities, through the entire PV system, of incoming photons with a certain wavelength according to their incident angle: a) λ=480nm (Blue); b) λ=520nm (Green); c) λ=620nm (Red); d) λ=820nm (Purple). The simplified model of a photovoltaic cell is assumed to have a glass protective cover placed right on top of a silicon substrate.

1.4.1. Panel's orientation

The orientation of a solar cell depends extensively on the reflectivity of the cell's surface; ideally mounted silicon solar cells are oriented in order to absorb the most sunlight. As shown in the previous section, reflection probability exceeds absorption probability at angles larger than 70° with respect to the cell's normal vector. Therefore, since, on average, 85% of the global solar irradiance is direct (Section 1.3), the angle between the imaginary line connecting the cell to the sun and the normal to the cell should be lower than 70° for the longest amount of time throughout a day and a year.

At higher latitudes, direct light has a high incident angle and it is less probable to reach solar panels without being scattered by particles in the atmosphere. Moreover, the percentage of reflected and diffuse light increases with large albedo-values. Diffuseness at high latitudes and reflectance due to surfaces with high albedo therefore play a bigger role for the orientation of PV modules.

1.5. Bi-facial solar panels

By focusing on the diffuseness of natural ambient light, a project on a revolutionary bi-facial photovoltaic system originated in the nineteen-sixties and resulted in the installation of the first prototypes about forty years ago [6]. Bi-facial solar panels (BFSPs) can indeed absorb light from every direction, if reflectivity losses at extreme incident angles (≥ 85°) are neglected (Figure 1.6b), as a result of the addition of an extra absorption face on the backside of standard mono-facial modules (MFSPs).

Figure 1.6a shows the structure of BFSPs, as opposed to that of mono-facial modules. Bi-facial solar cells have a similar structure to their mono-facial monocrystalline counterparts and, in most cases, the silicon wafer originates the same P-N junction[12]. However, bi-facial cells are enclosed within a symmetric system composed of an anti-reflection coating and a glass cover, as opposed to the glass-to-backsheet structure of MFSPs. Some bi-facial models have a transparent backsheet on the rear side instead of glass, therefore reproducing the structure of MFSPs.

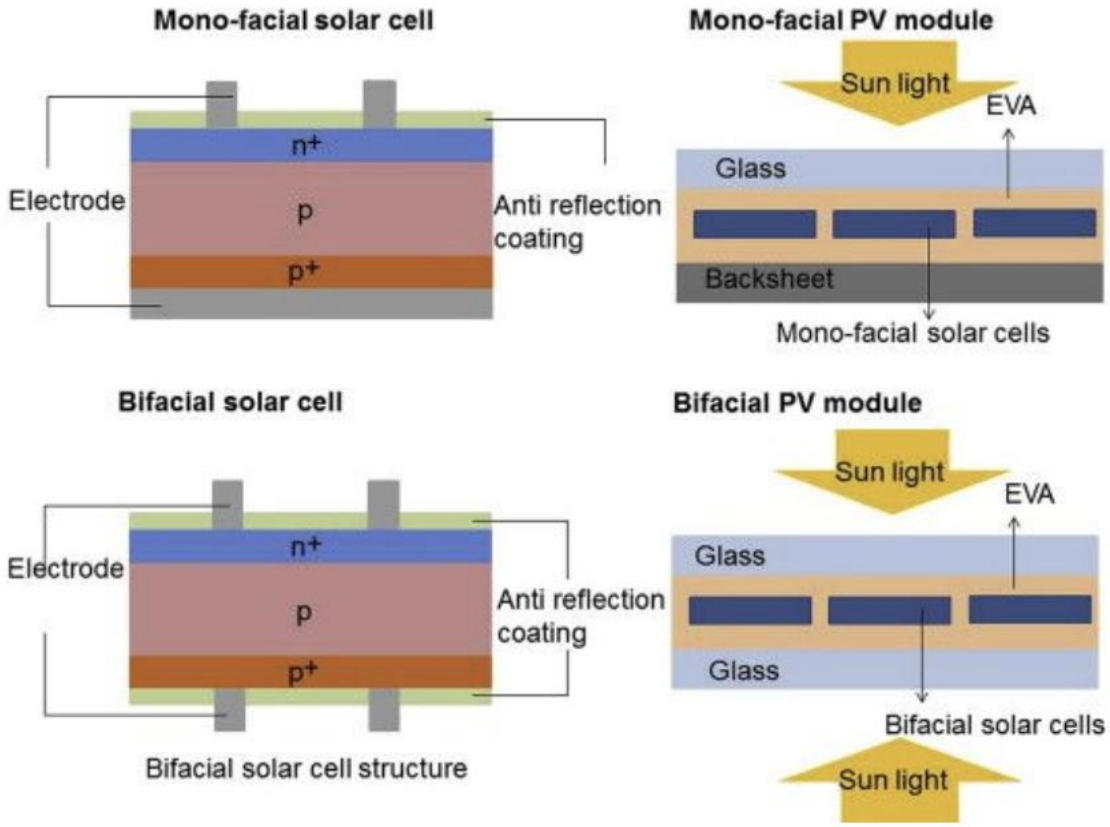

a)

[12] The junction between the p-type and n-type sides of the silicon.

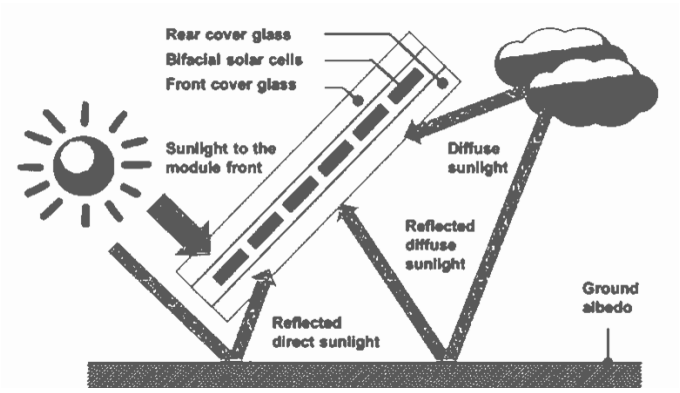

b)

c)

Figure 1.6a,b,c: a) The image shows the main differences between mono-facial and bi-facial solar modules. The depicted silicon cell is included in a transparent encapsulation film called EVA, as is the case for most bi-facial modules [28]. b) The image on the left shows the light contribution to a bi-facial solar panel [26]. c) The picture on the right shows vertically mounted (East-West orientation) bi-facial modules on the side of the highway A50, in the Netherlands [4].

1.5.1. Bi-faciality factor

Most bi-facial solar panels do not have a conducting back-sheet like silicon mono-facial modules. The resulting enhanced resistance in the flow of charge carriers is compensated by the addition of more conductors in the metal grid[13] of the rear side with respect to that of the front side [26]. This reduces the effective area available for sunlight detection on the back side with respect to the front. Due to the reduced area of the active layer, the back efficiency only reaches about 80 to 90% of the front efficiency. The bi-faciality factor is defined as the ratio between the nominal efficiencies[14] of the back and front faces of a BFSP. The bi-faciality factor is defined to be 80% throughout this analysis, according to the equal assumption made by Rodriguez-Gallegos et al. [24]. Recent manufacturing techniques have managed to exceed a bi-faciality factor of 95%, but most BFSPs available on the market have a 80% value [25].

1.5.2. Bi-facial energy gain

Since incident light is not unidirectional, the capacity of bi-facial SPs to absorb photons from all possible incident angles increases the flow of charge carriers inside the module and ultimately generates a gain in electric energy produced. The bi-facial energy gain represents the additional energy output generated by the back-side of a BFSP with respect to its front-side as compared to the energy yield of a mono-facial solar panel under the same conditions [30]:

$$G_{Bi\text{-}facial} = (Y_{Bi} - Y_{Mono})/ Y_{Mono} \quad (1.3)$$

[13] The metal grid of a PV system allows the DC current generated by the cells to flow towards the inverter.
[14] The PV nominal efficiency is calculated at standard test conditions. Standard test conditions are defined by: irradiation = 1000 W/m^2; cell's temperature = 25°C; air mass = 1.5. Air mass indicates the portion of the atmosphere the light must pass-through before being detected [21].

where "Y_{Bi}" and "Y_{Mono}" correspond to the electric energy yields of the bi-facial and mono-facial solar panels, respectively.

The energy-gain highly depends on diffuseness and on the albedo of the surrounding environment. The inclination and elevation, which determine the area shaded by the front face, together with the location on Earth are, therefore, particularly relevant to the analysis of the bi-facial gain.

1.5.3. Cost-efficiency

The higher expenditures of bi-facial systems, with respect to those of standard mono-facial systems, have played a major role in the underdevelopment of bi-facial technologies with respect to MFSPs. As the similar structure of the two system suggests (Figure 1.6), the fabrication process of the two module types is very similar and Rodríguez-Gallegos et al. estimate the current average fabrication costs of BFSPs to be only 11.2% higher than those of MFSPs [24]. The dropping costs of solar cells per unit of energy generated[15] have induced the development of new manufacturing techniques that aim to decrease the economic difference between MFSPs and BFSPs [16]. All the other costs related to the panel's maintenance and operation are approximately equal for the two types and depend on the specific country of interest [24].

Further research on the effects of ground albedo, panel's inclination and orientation on the bi-facial gain stimulates the proliferation of BFSPs; these are expected to reach two-fifths of their mono-facial counterparts' world share in the same year by 2028 [22].

1.6. Methodology

This project evolves from the data analysis of a prototype device, the "light ambiance detector" or simply "LAD", situated next to the AMOLF solar field, outside the AMOLF building in Science Park, Amsterdam. The LAD is a multi-directional light detector that measures irradiance values of incoming light in different orientations every ten seconds. The collected data provide the empirical background to the location-specific cost-efficiency analysis of bi-facial SPs with respect to mono-facial modules. The approach to this cost-efficiency analysis follows the method advanced by Rodríguez-Gallegos et al., which is based on the derivation of the levelized costs of electricity for the two solar systems [24].

The relevance of this cost-efficiency analysis corresponds to the evaluation of the best compromise between bi-facial and mono-facial solar panels' efficiencies and costs. The advancement of an accessible method to confront the two systems could successfully guide potential buyers through the choice of the best solar module, eventually increasing the global amount of SPs and sustainable energy produced.

[15] The levelized cost of electricity of solar cells has decreased by 88% since 2009, the greatest drop among all renewable energies [7].

Chapter 2

The LAD

The LAD is a multi-directional light detector that evolves from the previous rudimentary apparatus with similar functions, the AMOLF "cube" [17] (Figure 2.1). The "cube" project initiated from the interest in the analysis of diffuse light: by measuring solar irradiance values from six faces disposed in a cubic arrangement, the "cube" was able to detect data on indirect irradiation. It became the first AMOLF prototype to detect light with sensors that were not facing the sky, therefore providing additional information with respect to the data obtained by the AMOLF spectroradiometer[16]. Its accuracy, proved in comparison to the data of the sun tracker at ECN [17], encouraged the design of a second device, the LAD.

The LAD's project commenced with Kersten's analysis of the best configuration for the detection of light incoming from any direction [14]. By increasing the number of sensors from six to twelve, the precision of the diffuseness measurement greatly improved and its expected discrepancy with respect to a measurement obtained using an infinite number of sensors was projected to be, on average, only 4% [14].

[16] The AMOLF MS-711 Spectroradiometer is a light detector, which measures irradiance values, between 300 and 1100nm, with a field of view of 180° (only the hemispheres above it). Its specifics can be found at [8]: https://eko-eu.com/products/solar-energy/spectroradiometers/ms-711-spectroradiometer/pdf

Figure 2.1a,b,c: From the top-left: a) The picture shows the "cube" being placed in the solar field at AMOLF [17]. b) and c) The pictures show the LAD in the AMOLF solar field: the first image is zoomed on the detector; the second image shows the entire solar field, in which the LAD and the spectroradiometer (white) can be identified on top and on the bottom of the second panel from the left, respectively.

2.1. Characteristics

The twelve sensor boards are disposed in a dodecahedral geometry, which is enclosed into two attached transparent PMMA hemispheres[17] of about 30cm in diameter. Each sensor board is situated at the center of one of the twelve faces and includes a temperature sensor and four diodes. The diodes measure irradiance values for the ranges of the light spectrum corresponding to blue, green, red, and infrared [1]. The plastic enclosure protects the sensors from all weather conditions and UV radiation, and contributes to about 20-30% of the reflectivity losses of the radiation reaching the LAD's sensors (Figure 2.4). The shading due to the ring between the two plastic hemispheres (Figure 2.2b) constitutes

[17]PMMA, or acrylic, is a type of plastic. The specifics of the hemispheres can be found at: https://nl.aliexpress.com/item/32332234092.html?storeId=1776056&spm=a2g0z.12010612.0.0.10ba8e21hrDItH

a small error to the detection of indirect irradiance as compared to the accuracy gain of the LAD with respect to the "cube" and is thus not taken into account in the model [14].

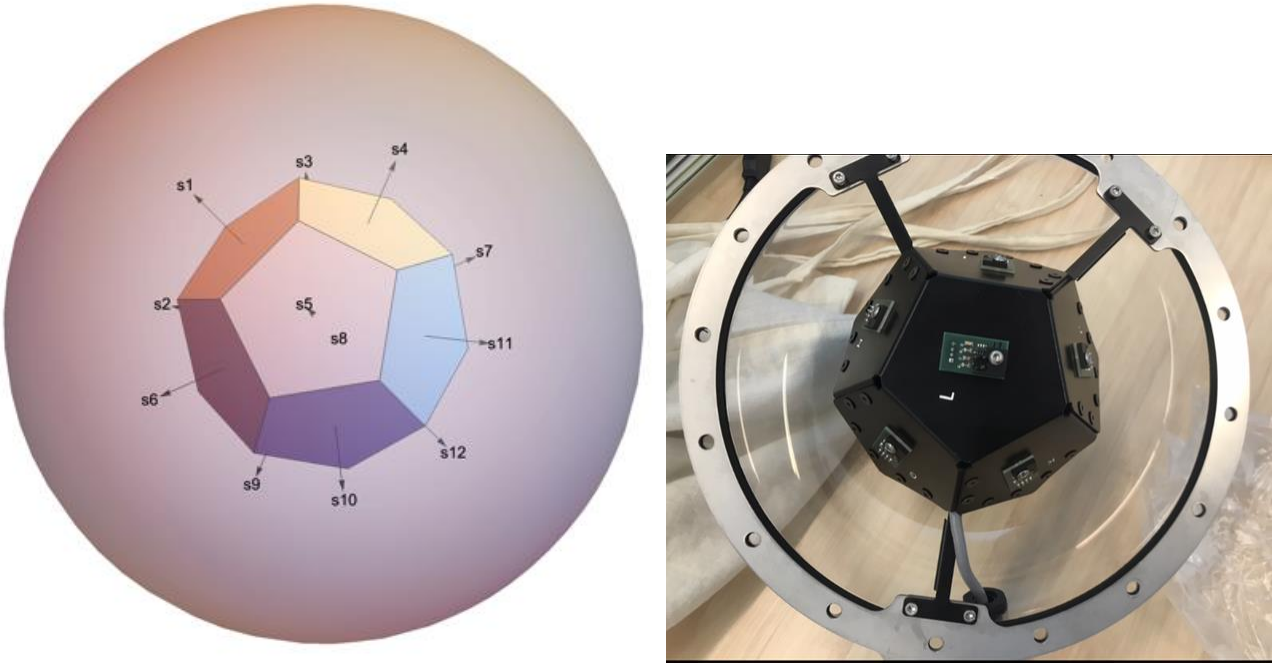

Figure 2.2a,b: a). The Mathematica simplified graphical representation of the LAD. The position of the sensors is identified by normal vectors to them. The face containing sensor 1 ("s1") has the same inclination and orientation of the other panels of the solar field. It is assumed here the same perspective of Figure 2.1c. b) A close-up picture of the back-side of the LAD with sensor-board 12, or "L", in the fore-ground; the lower plastic hemisphere was detached before the picture was taken.

2.2. Data read-out

A fundamental step of the analysis of the data detected by the LAD is the conversion of the raw output, which the sensors return, into irradiance values, in units of Watts per meter-squared.

2.2.1. Converted output

The conversion program was developed by the AMOLF intern Simon Voogel for the benefits of this project. Simon integrated the conversion functions, which were derived at the end of the sensors' calibration process (Section 2.2.2.2.), into a program in LINQPad[18]. Given a set of the LAD' s raw data, which can be downloaded from the solar field storage on the AMOLF server, the LINQPad program returns a converted set. The outcome is a list of data corresponding to a specific date and time of detection, which includes, for each sensor, the irradiance values [W/m^2] of the 4 diodes and the corresponding sensor's temperature.

[18] LINQPad is a software free to download on Windows computers at: https://www.linqpad.net/download.aspx. The program developed by Simon can be found at: https://drive.google.com/file/d/1-K0c9uEJWch8NkjharZXGwYkctKEd5me/view?usp=sharing

2.2.2. Calibration

Before being installed on the LAD, each sensor board was calibrated under a solar simulator[19], as part of my internship project at AMOLF, in the Fall of 2018. The method used for the calibration follows Kersten's approach [14].

The sensors were tested at selected temperatures and intensities in order to obtain functions of the raw output over actual irradiance values (Section 2.2.2.1.). A diversified range of temperatures, 3.8°, 31°, 37.5°, 60°, and 76°, and solar intensities, 48.3 W/m^2, 127W/m^2, 274W/m^2, 295.6W/m^2, 371W/m^2, 503.8W/m^2, 734.8W/m^2, 744W/m^2, 755.4W/m^2, 867W/m^2, 988.1W/m^2, and 1145.4W/m^2, were considered in order to simulate different weather conditions.

For measurements at low temperatures (3.8°C), de-ionized water and ice were used, while high temperatures (60°C and 76°C) were achieved through the use of a 10Ω resistor, which was attached to the sensor boards via a heatsink. For measurements at low intensities (47-48 and 126-127 W/m^2), a neutral density optical filter[20] was placed on top of the sensors, in order to decrease the incoming irradiance to about 10% of the intensity at the source.

The raw data can be found at:
https://drive.google.com/file/d/1nnq0j6qAOjp4AIvykBdgWxz9SYnVGh9j/view?usp=sharing, where detected temperatures are in degrees, the registered raw output is dimensionless, and the input intensities are expressed as fractions of 1 Sun, or 1000W/m^2.

2.2.2.1. Linear plotting

The raw data from the sensors were plotted as functions of the solar simulator's intensity for the given temperatures; a linear regression was assumed. The Mathematica[21] codes and the obtained graphs of the linear functions can be found at:
https://drive.google.com/drive/folders/1qnm8nUTBr10TuC0ETvmXTWkcnfKWSNX0?usp=sharing.

2.2.2.2. Inverted linear equations

The linear equations obtained in Section 2.2.2.1. are of the form:

$$raw\text{-}data = a*intensity + b \qquad (2.1)$$

Each a and b depends on the specific sensor board, color, and temperature as shown by the files at: https://drive.google.com/drive/folders/1gpHIlqcnNXyfLLlU-FkK1-F4BAK-9q8n?usp=sharing. By ignoring the b parameter and inverting equation 2.1 obtained for every sensor, color, and temperature, the

[19] The solar simulator has a 1.5G air mass filter, which resembles the typical AM1.5 global radiation spectrum, which is the standard spectrum at the Earth's surface.
[20] The filter's specifics can be found at: https://www.thorlabs.com/thorproduct.cfm?partnumber=NE205B.
[21] Throughout this paper, the possession of the 11.3 version of Wolfram Mathematica is assumed for the correct visualization of the codes.

converted data (W/m^2) result from dividing the initial raw data by the corresponding a. The conversion functions for each sensor and color are grouped at:
https://drive.google.com/file/d/1nuekkg0B55w_VrIWepawPHIedNdIx9Pb/view?usp=sharing.

The b's of equation 2.1 are not considered in the conversion since the linear equations obtained in Section 2.2.2.1. should have a zero-offset; the raw output of the sensors associated to a 0 W/m^2 irradiance should indeed be null. The observed off-set is a result of a measurement error per se and, potentially, of the non-linearity of the conversion function.

2.2.3. Accuracy of conversion

The system of conversion functions developed through the sensors' calibration is not flawless. The values of b, indeed, fluctuate between very high positive and negative numbers in the linear functions obtained by calibrating the sensors at different intensities and temperatures. By calculating the standard deviation of the b's for each temperature and sensor and comparing it with the conversion functions, an accuracy analysis[22] was developed. The results show that the conversion functions developed in Section 2.2.2.2. lose relative accuracy with decreasing irradiance, due to the high values of (b) with respect to (raw-data/a), when the raw intensity data are small. The trend observed in every sensor board is that the precision of the converted data falls below 70% when irradiance values are lower than about 140W/m^2. This result suggests a significant level of inaccuracy for the data measured by the LAD during most hours of the day.

The undesired off-set of equation 2.1 is partly due to instrument and measurement errors during the calibration process. The fluctuations of the solar simulator's irradiance values reduced the accuracy of the intensity determination. Furthermore, during the calibration, the sensor boards did not always align with the center of the solar simulator's lamp. The imprecise placement of the sensor boards influenced the precision of the calibration, since the sensors' responsivity is dependent on the angular displacement of incoming light as shown in Figure 2.3.

The off-set of equation 2.1 is also partly due to the assumption of the linearity of the conversion equation. Indeed, the calibration measurements do not correspond perfectly to the fitting lines of the corresponding sensors, temperatures, and colors. The standard deviation of the b's corresponding to each sensor was shown[23] to be smaller than the standard deviation of the residuals of the fitting lines of the different colors and temperatures for the corresponding sensor.

[22] https://drive.google.com/file/d/1N4epXv-PvweGeY23No7vwazeemhtTAPg/view?usp=sharing.
[23] At the end (Section 3) of https://drive.google.com/file/d/1DP30ov3EYHsh0XzOvNiJMMPfEgzXNN0c/view?usp=sharing.

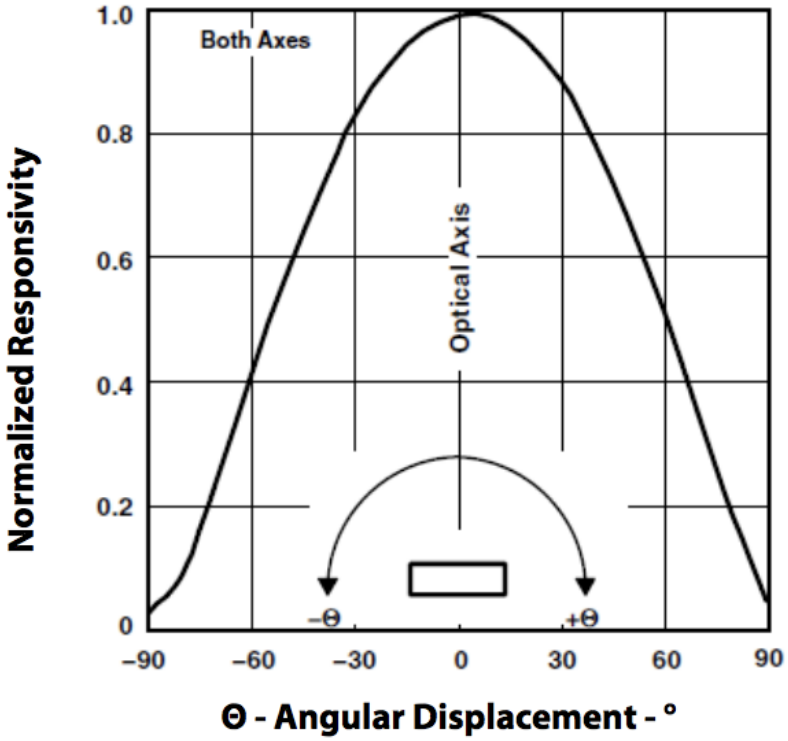

Figure 2.3: The plot [1] shows the normalized responsivity of the LAD's sensors as a function of the angular displacement from the normal to the sensor board. Kersten demonstrated that this curve fits almost perfectly to a cosine curve [14].

2.3. LAD vs. Spectroradiometer

The project on light ambiance detectors initiated at AMOLF as a way to investigate the solar radiation reaching an object from every direction. In the AMOLF solar field, data on weather and light intensity are collected by a spectroradiometer, which only has a field of view of 180 degrees. The installation of the LAD, after the successful outcome of the "cube", therefore increases the field of view and promotes a more meticulous analysis of indirect irradiation.

The accuracy of the spectroradiometer's measurements is superior to those of the LAD. Indeed, aside from the low conversion precision at low intensity values (Section 2.2.3.), the sensor boards of the LAD underestimate the incoming radiation, since more light is reflected at the spherical plastic around it than at the quartz cover of the spectroradiometer. However, the analysis of the ratio between the intensities measured by the LAD's opposite hemispheres provides information on the indirect light contribution to the total solar radiation that is basically unknown to the spectroradiometer.

2.3.1. Reflectivity losses

The refractive index of the spherical PMMA surrounding the LAD is higher than that of the quartz cover surrounding the spectroradiometer, thus causing a difference in reflectivity losses [3]. Light

reaching the LAD's plastic spherical surface gets reflected according to the angle of incidence (AOI) with respect to the radial vector. The transmitted ray, according to Snell's laws of refraction, leaves the inner part of the sphere with an angle equal to the AOI [9] and is eventually detected by one of the twelve sensor boards.

The transmittance probability for the air-plastic-air system is shown in Figure 2.4. In the analysis of the system, the spherical surface is assumed planar, since the wavelength of the incoming photons is much smaller than the thickness of the plastic; the angle of curvature corresponding to the incident light is also almost null.

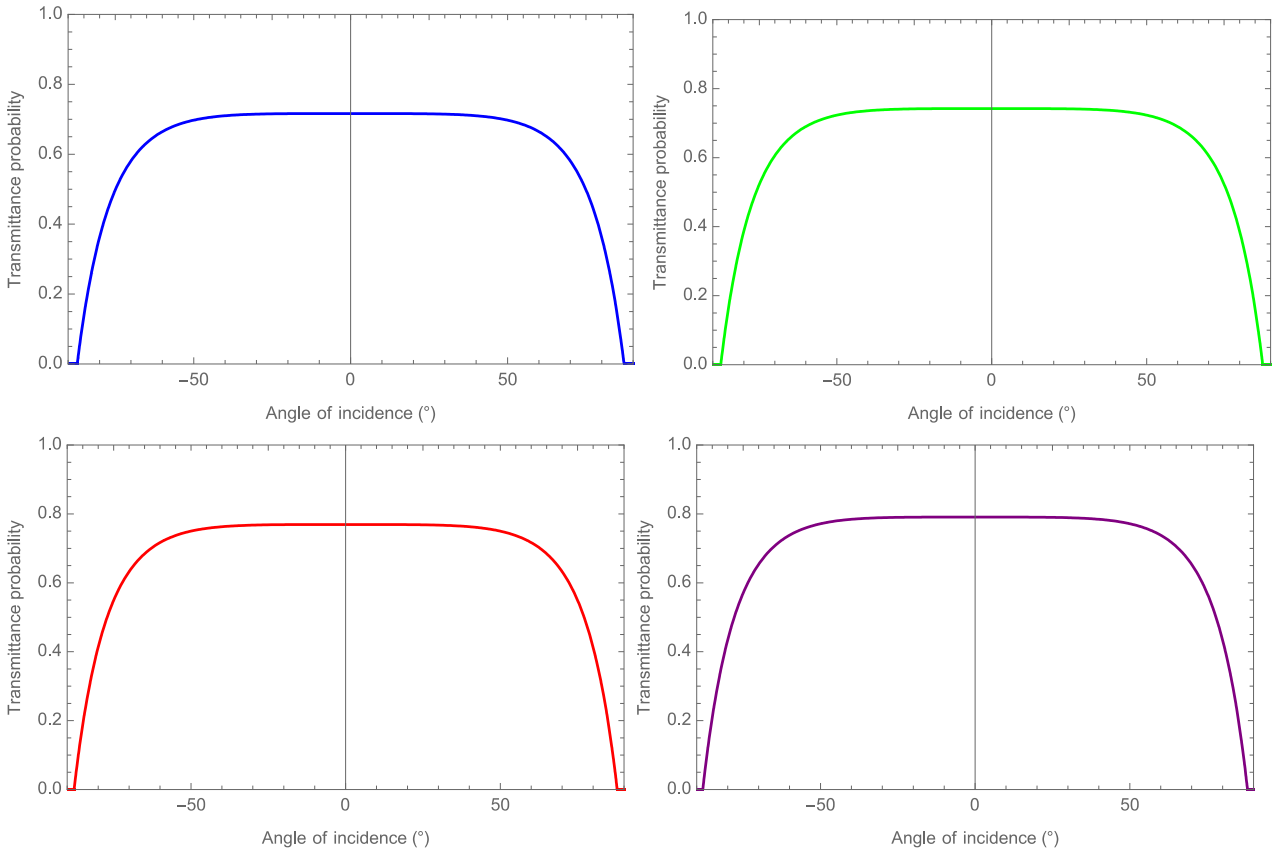

Figure 2.4: The line graphs show the transmittance probability through the spherical cover of the LAD of the incoming light as a function of the angle of incidence. The different colors correspond to the diodes in the same way as in Figures 1.4 and 1.5. The infrared diode has a transmittance probability of about 80%, while the blue diode of only 70%.

The distance from the center of the LAD to any of the sensors is about 5cm and the radius of the sphere is about 15cm. The light that gets transmitted through the plastic and reaches any of the sensors, leaves the inner sphere with an angle lower than 20 degrees. Indeed, the angle of incidence on the sensor is maximum when the light reaches it along its horizontal plane; the sine of such angle, measured as the ratio between the vector connecting the center with the sensor and the radius, is about 1/3. Figure 2.4 shows that the irradiance detected by the sensors, for AOI lower than 40°, is between 20% and 30%, according to the photons' wavelength, less than what would have been measured in the absence of a plastic spherical cover.

The normalized responsivity of each sensor board, as a function of the angular displacement, is reduced by about 20-30% due to reflectivity losses at the spherical plastic around the LAD, while the spectroradiometer's responsivity corresponds to Figure 2.3 reduced by less than 5%, as indicated in the instrument's datasheet[16] above. However, the systematic error due to the LAD's reflectivity losses is ignored when considering only the ratios between irradiance values.

2.4. Graphical visualization of detected irradiance

The daily irradiance detected by each face of the LAD provides decisive information on the directionality of incoming sunlight over time. The investigation of the sensors' relative intensity differences underlies a primitive evaluation of the faces detecting the most intense direct light and of those detecting only indirect radiation. The contribution of direct and indirect light, during a specific day, is effectively perceived in the graphical visualization of the irradiance values as a function of time and sensor, since the former does not reach the back faces. Figure 2.5 shows the plots of the irradiance values detected, every 5 minutes, by the four different diodes of each sensor for a sunny and a cloudy day.

a)

Sensor 1

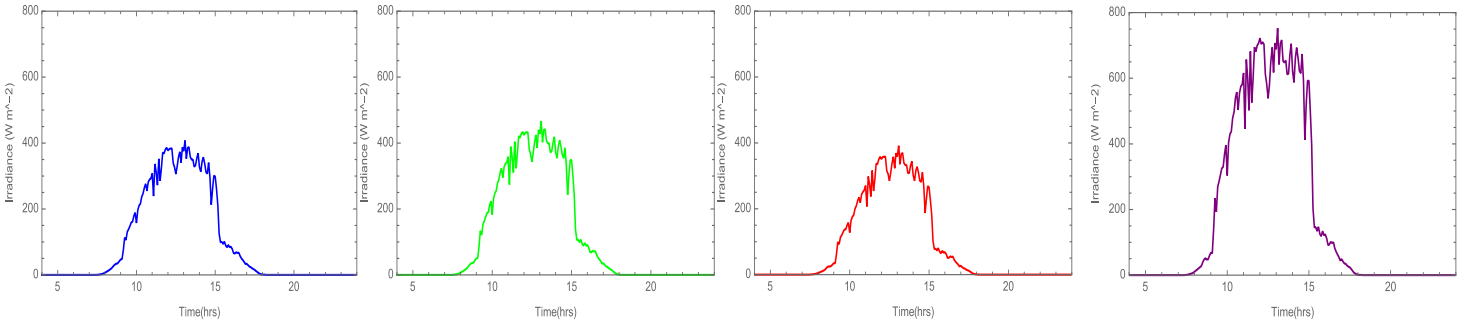

Sensor 2

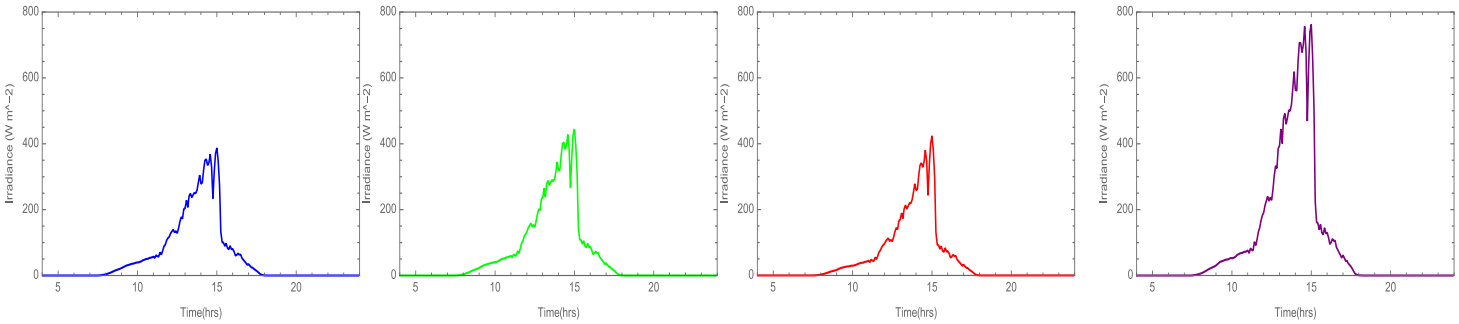

Sensor 3

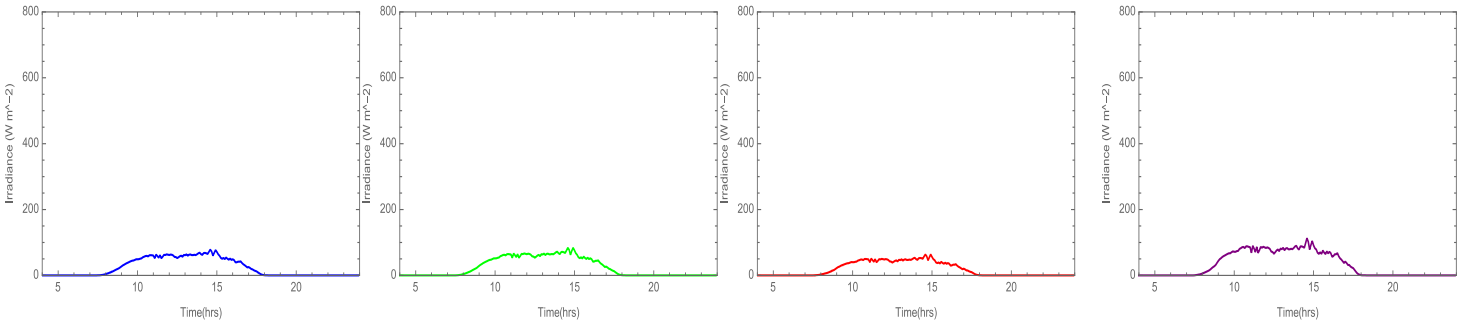

Sensor 4

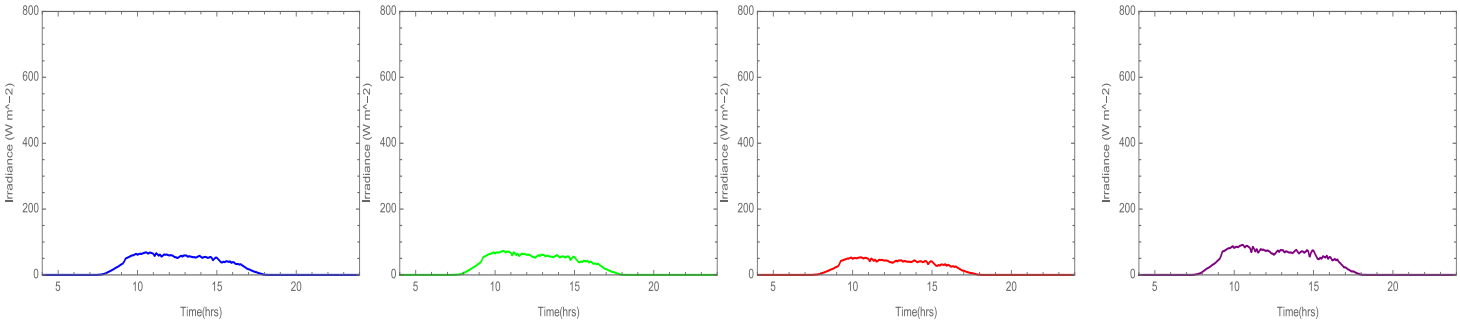

Sensor 5

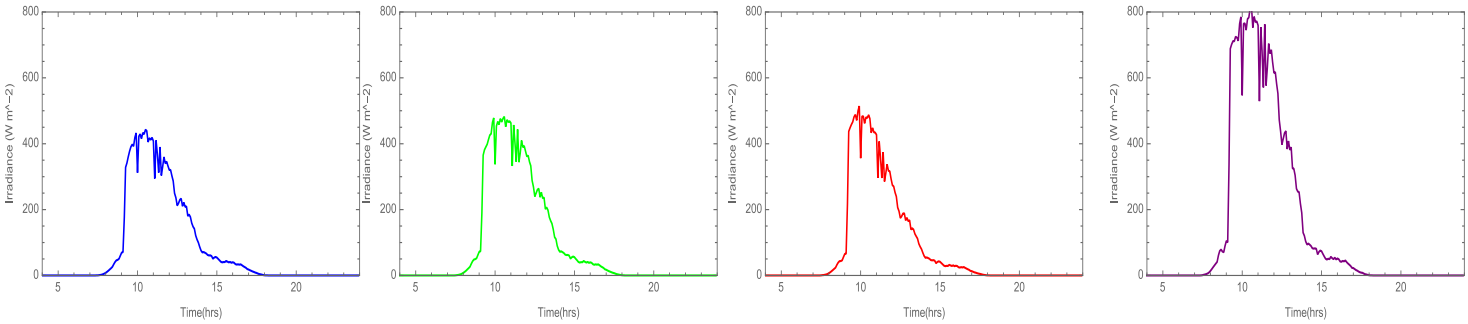

Sensor 6

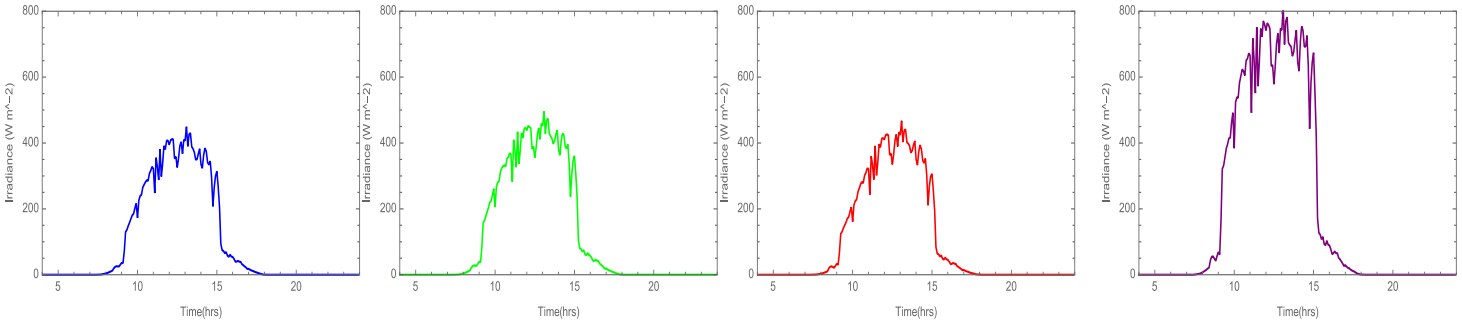

Sensor 7

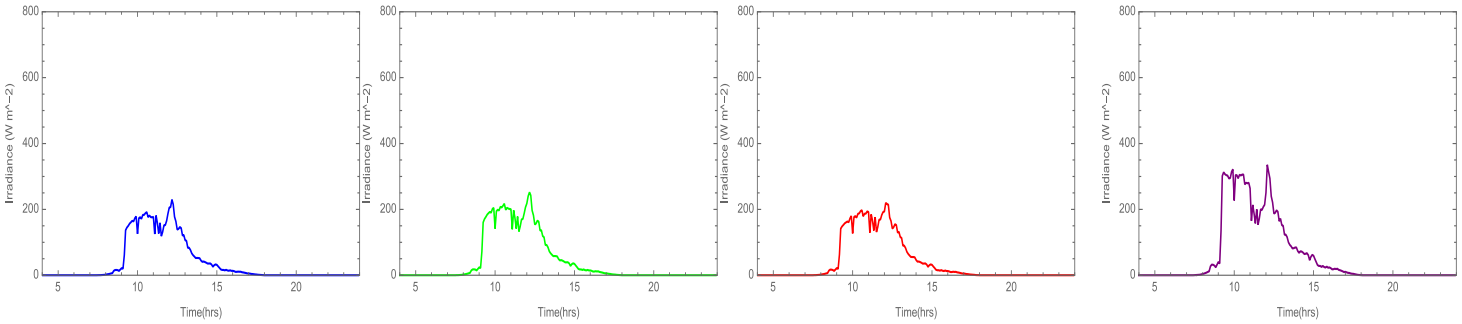

Sensor 8

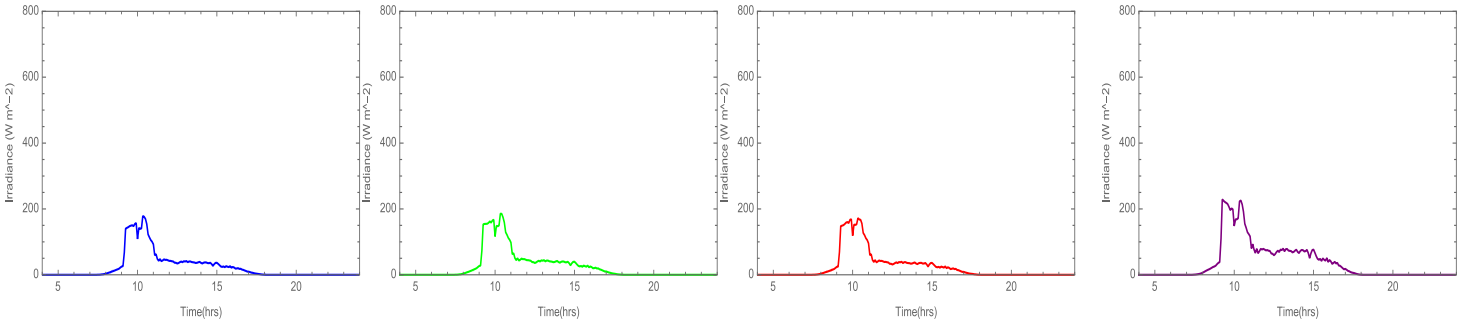

Sensor 9

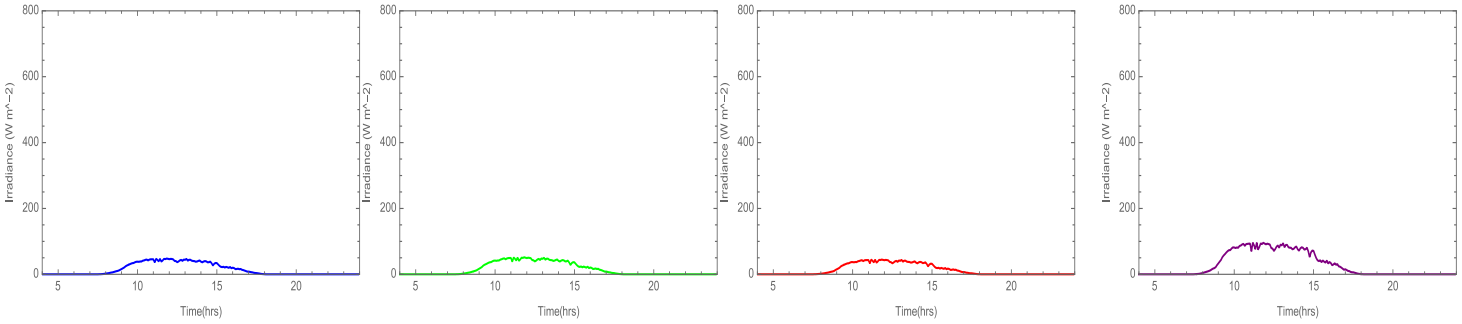

Sensor 10

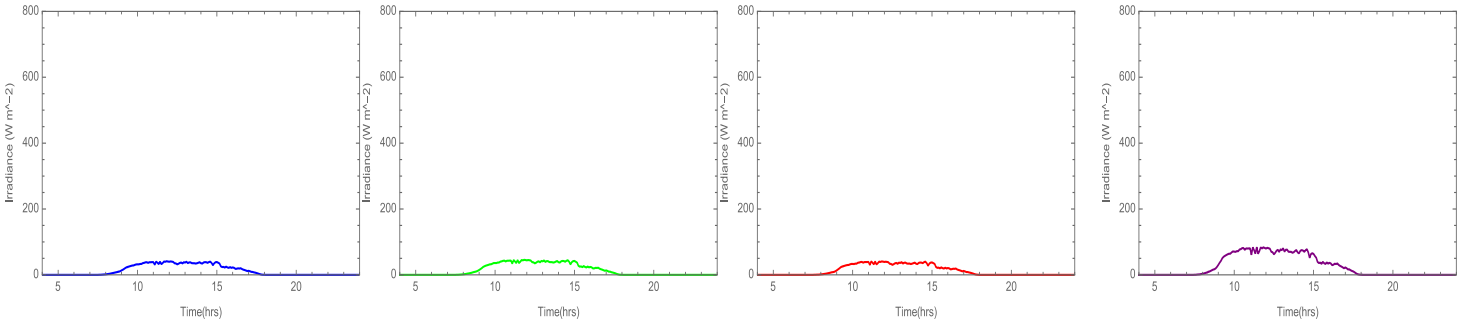

Sensor 11

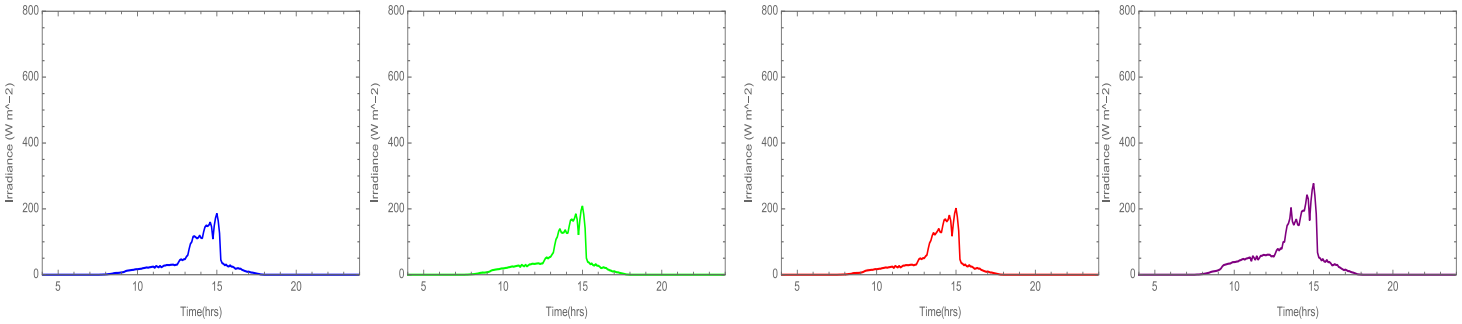

Sensor 12

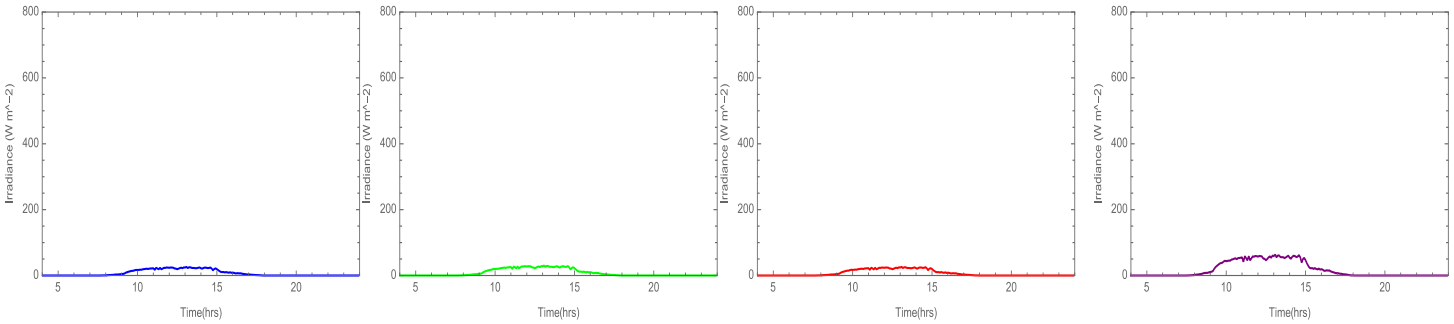

b)

Sensor 1

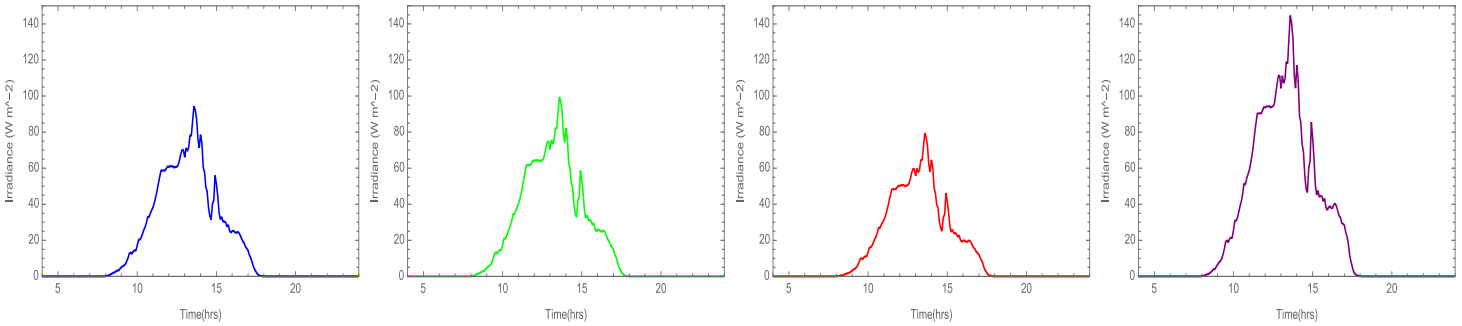

Sensor 2

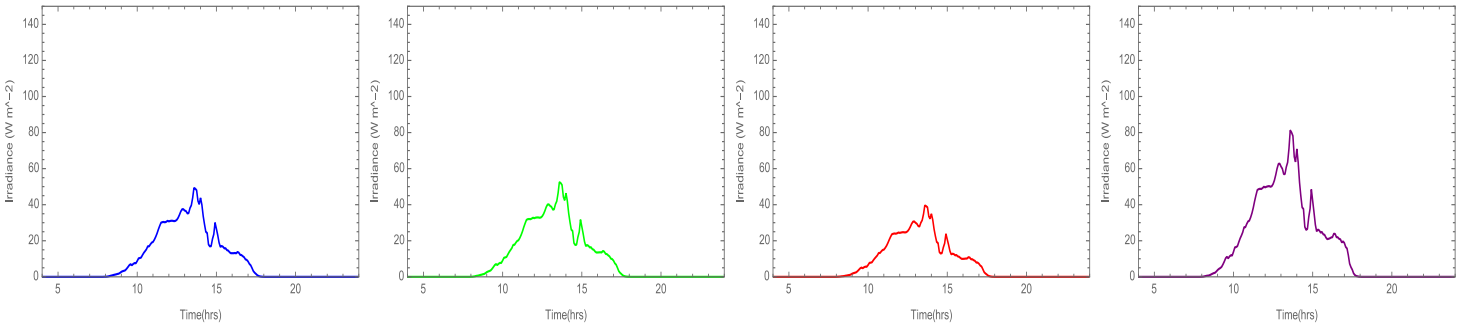

Sensor 3

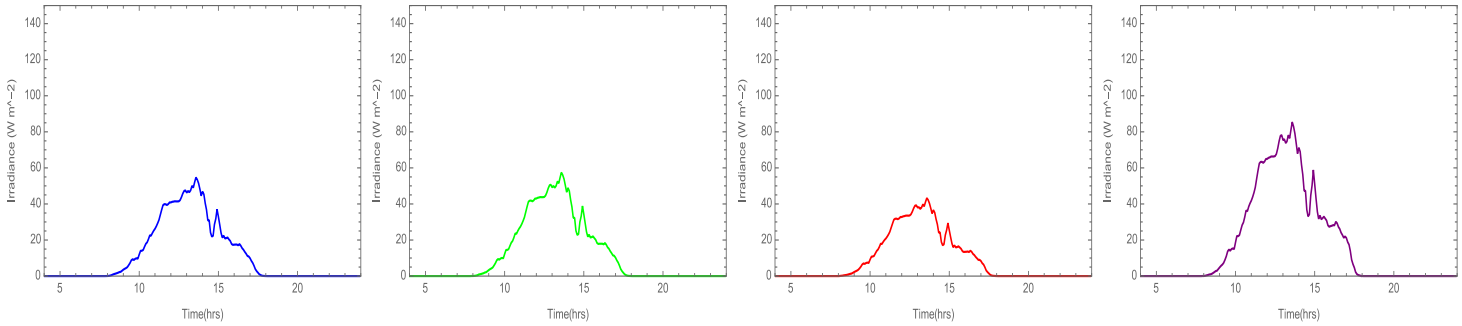

Sensor 4

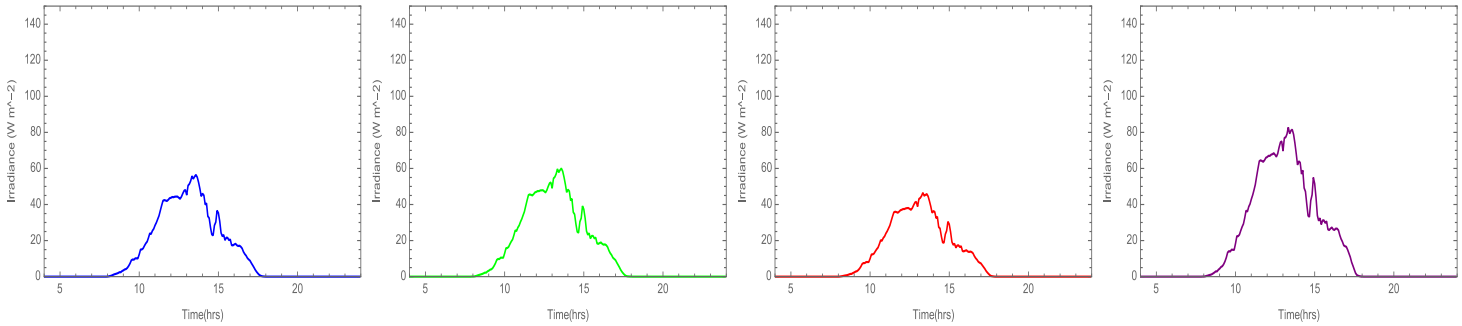

Sensor 5

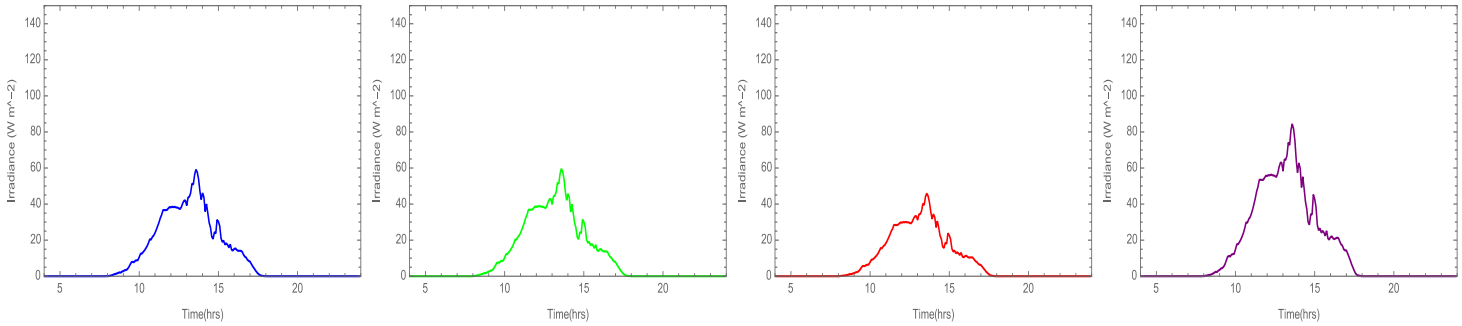

Sensor 6

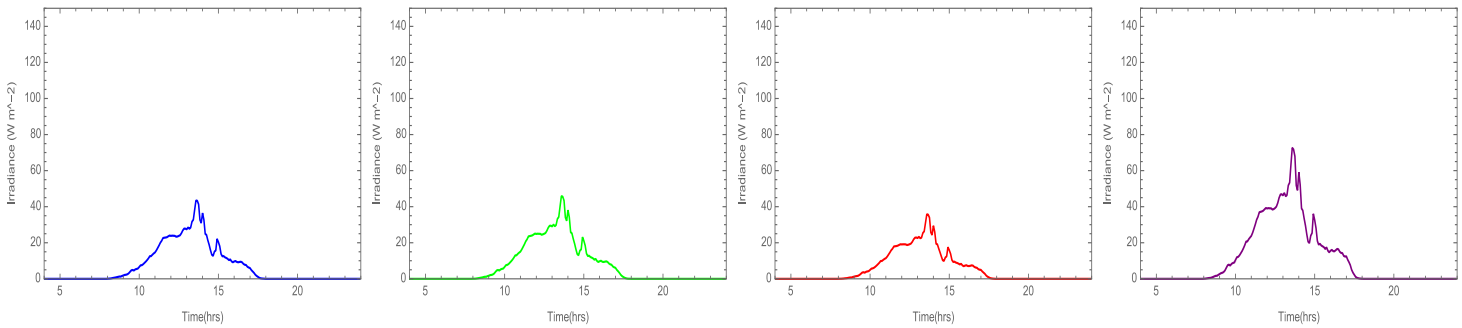

Sensor 7

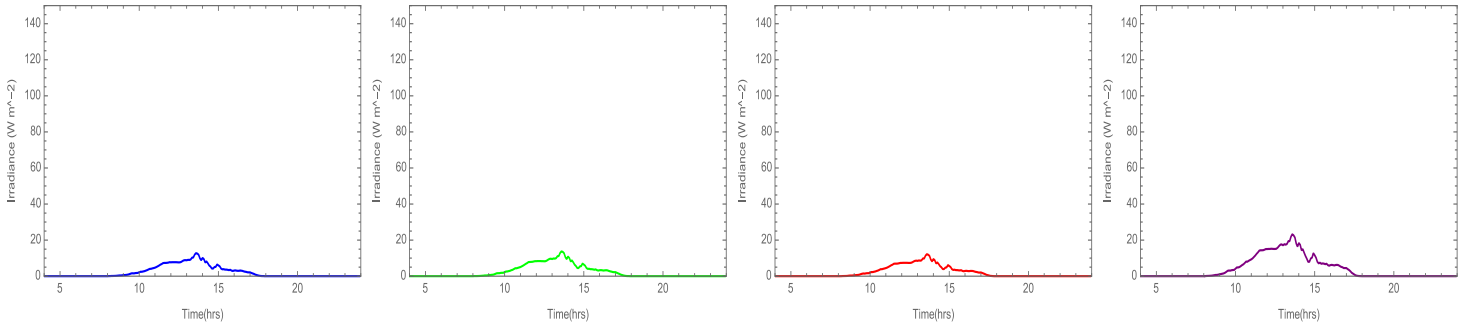

Sensor 8

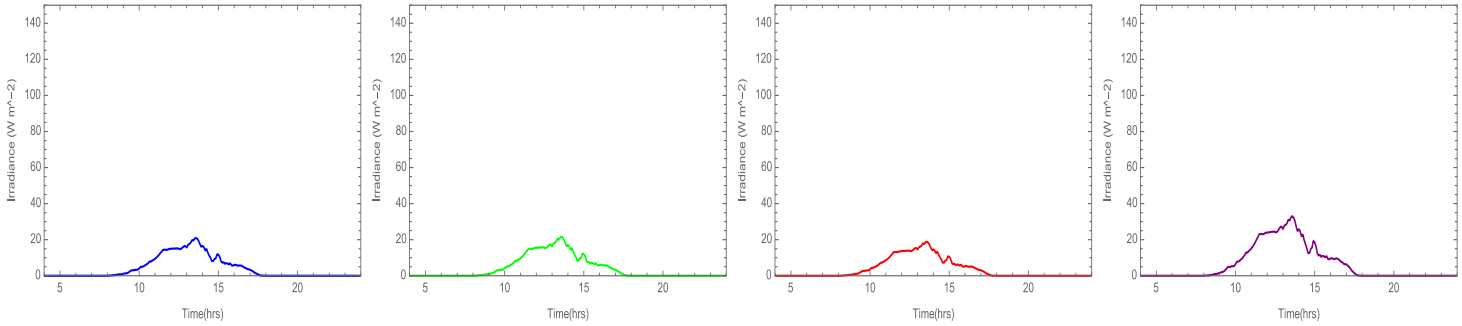

Sensor 9

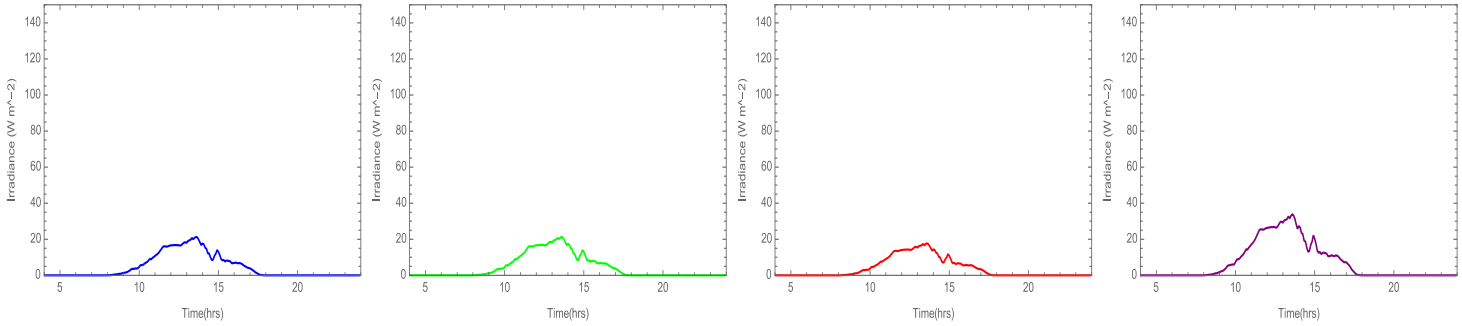

Sensor 10

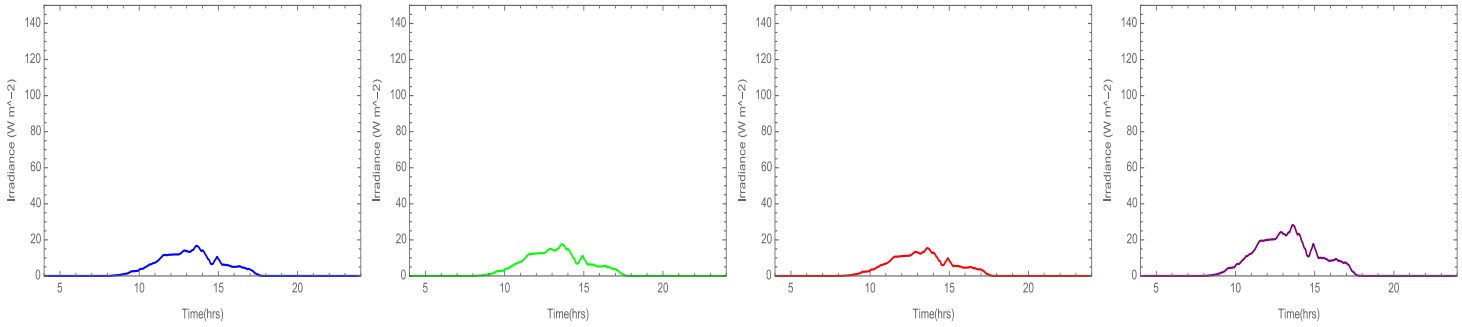

Sensor 11

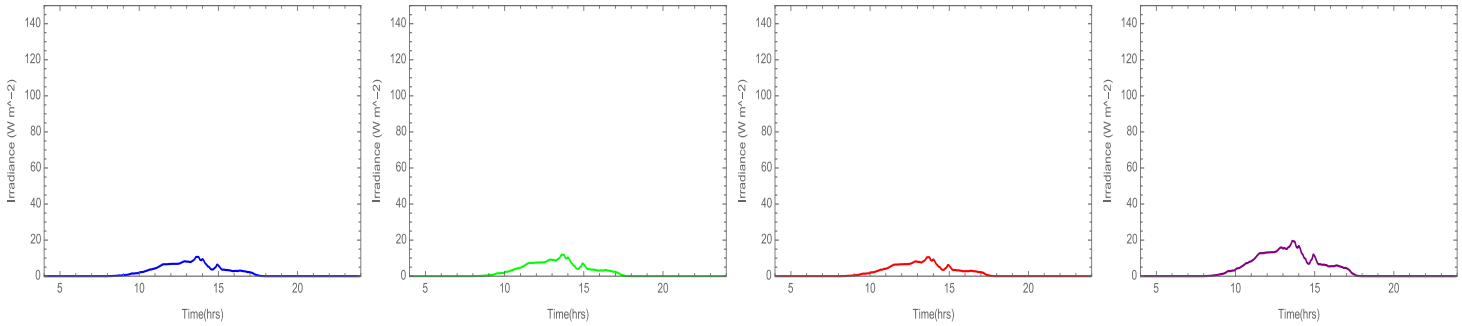

Sensor 12

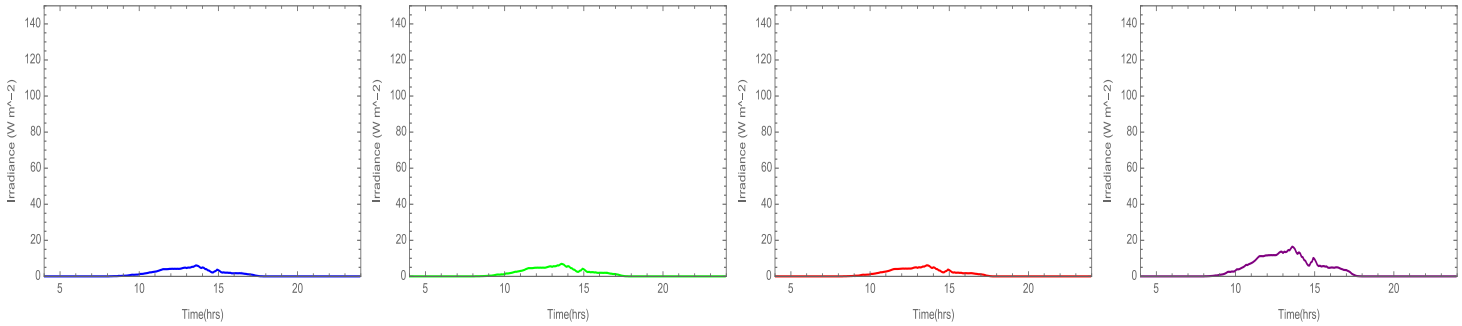

Figure 2.5a,b: The graphs show the irradiance values measured by the 4 diodes of each sensor on a sunny day (18th of February 2019) (a) and on a cloudy day (2nd of February 2019) (b). The observed shapes of irradiance oscillations, for each sensor, are similar for all wavelengths; however, the infrared diodes, and in particular those located in the upper hemisphere, registered higher intensity values on both days, since they have a higher spectral responsivity. The time range is from 4am to 11:55pm; the maximum irradiance on the y-axis is 800 (W/m^2) for figure 2.5a and 150 (W/m^2) for figure 2.5

2.5. The LAD for the inclination of PV modules

Section 2.4 delineates the particularly important function the LAD serves: it indicates the faces that receive the most intense[24] incoming light throughout a day. The directionality of incident light is fundamental for the consideration of the optimal inclination of a solar panel, since this should point towards the direction of the most intense radiation for the longest amount of time (Section 1.4.1.).

The solar radiation measured by each of the LAD's diodes is assumed, for simplicity, as incident on the LAD's faces perpendicularly to the plane of the sensor boards. By multiplying the solar irradiance values by the unit normal vectors of the corresponding sensors and by summing up the results for the 12 faces, the resulting vectors indicating the direction of the most intense incoming light are obtained. Figure 2.6 shows the vectors resulting from the irradiance detection every 5 minutes, for both a sunny and a cloudy day.

[24] By most intense, the maximum power over a surface, on which the light is incident, is intended.

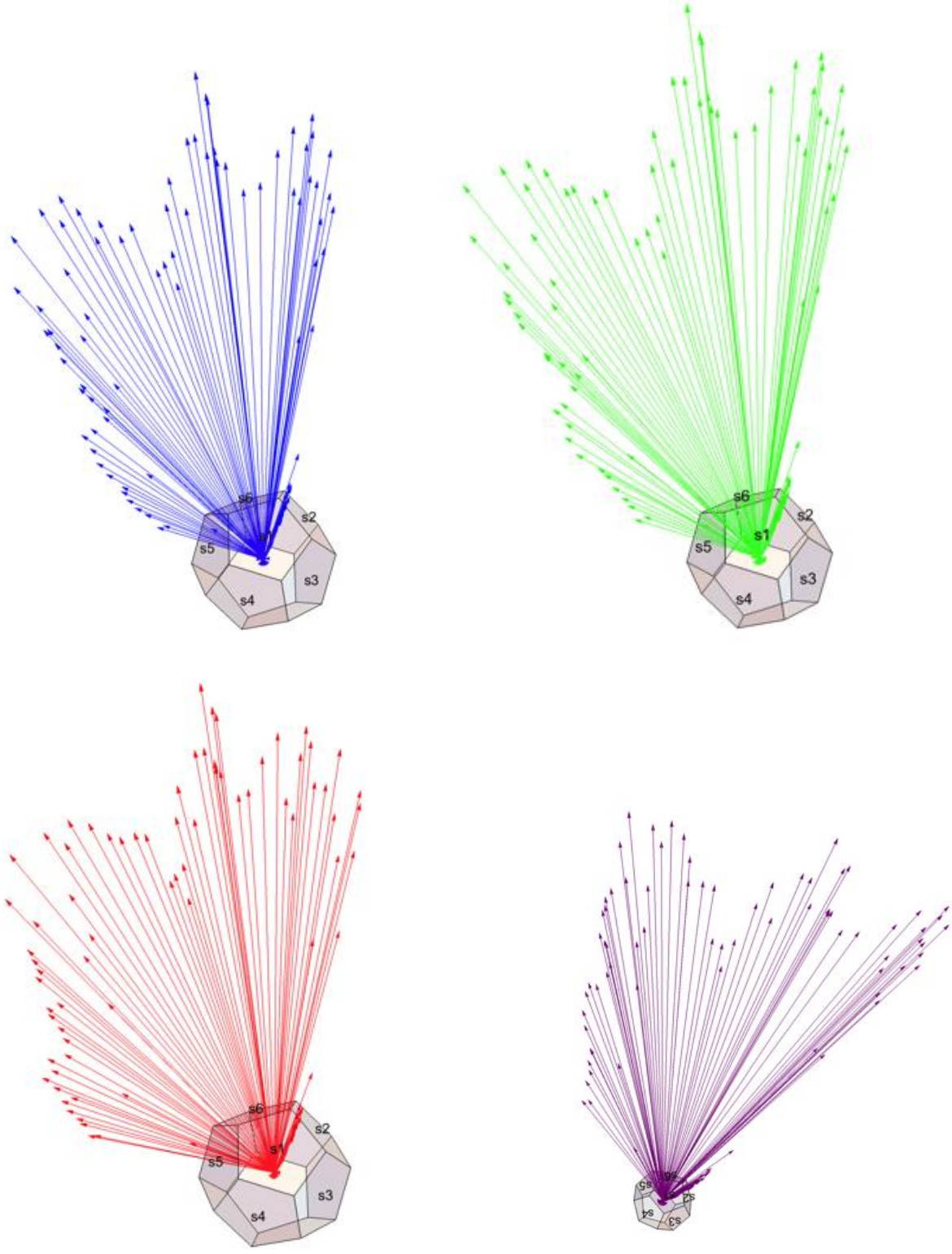

a)

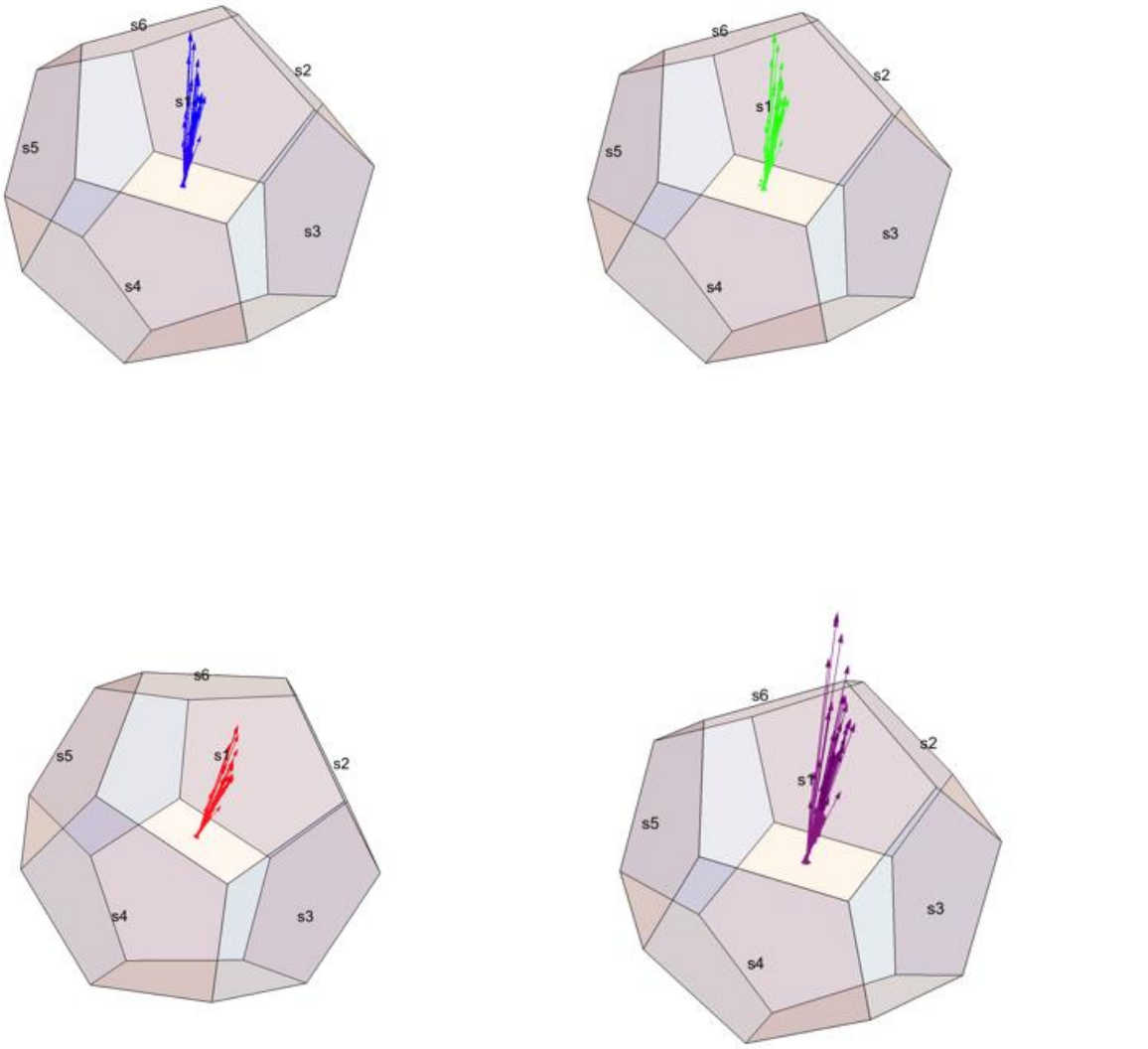

b)

Figure 2.6a,b: a) The first four images show the vector sums on the 18th of February 2019, a sunny day; b) The last four images depict the vector sums on the 2nd of February 2019, a cloudy day. The images are represented here according to a common point of view. Infrared light is the most intense, as already shown in Figure 2.5.

Following from Figure 2.6, the magnitude and direction of the radiation vector sums provide information on the diffuseness of sunlight, throughout any given day. Long vectors all converging on the uppermost faces of the LAD suggest a prominent portion of direct incoming light, while shorter vectors indicate a lower overall intensity, which suggest a higher share of diffuse and reflected light.

Chapter 3

Energy Analysis

Indirect light is essential for the energy gain of bi-facial solar panels with respect to standard mono-facial modules. This chapter investigates the energy gain that a BFSP would have if it was placed in the AMOLF solar field. The AMOLF monocrystalline heterojunction silicon solar module[25] (HIT Si) represents the reference standard mono-facial panel of this energy analysis, while the LAD provides information on the rear side of a BFSP whose front side is assumed to have similar optical and efficiency characteristics to the HIT Si panel.

The influence of inclination, elevation, and ground albedo on the bi-facial gain is excluded from this analysis, which assumes, for the BF panel, the same setting of the current LAD's position, as displayed in Figure 2.1c and Figure 3.1. The short distance between the LAD and the HIT Si panel minimizes any possible difference in incoming solar irradiance detected by the front side of the BFSP and the MFSP.

Furthermore, the possibility to easily move the LAD to different locations, suggests the applicability of the following method in other circumstances.

[25] The module is portrayed as the second panel from the right in Figure 2.1c. The panel's datasheet can be found at https://drive.google.com/file/d/0B5ISkJCV7rkaS3NFcUR5QU5tMU5HZE1Rcjc3dDFXV2tJSUxv/view?usp=sharing.

Figure 3.1: The image shows the surface background behind the AMOLF solar field. The presence of concrete, grass and shade from the near tree complicates the calculation of the albedo value, which influences the reflected light detected by the rear side of the LAD. A rough estimate constrains the albedo value between 0.1 and 0.2.

3.1. Methodology

This chapter only considers the relative difference of the energy yields of the bi-facial and mono-facial modules (Equation 1.3); the ratio, rather than the absolute value, of the energy outputs of BFSPs and MFSPs is therefore addressed.

3.1.1. Energy yields

The energy outputs of the two PV modules are derived from the solar irradiance detected by them. The solar radiation, if multiplied by the surface area of the panels, corresponds to the solar power a module receives. The power output is then given by the incoming solar power multiplied by the efficiency of the cell. Finally, the energy yield corresponds to the power output integrated over the amount of time during which that electric power was generated.

3.1.1.1. Irradiance

The incoming irradiance detected by the BFSP and MFSP is given by the data collected by the LAD. In Chapter 3, the total irradiance detected by each sensor board is assumed to be equal to the sum of the values obtained by its four diodes. The spectral responsivity of the sensor boards [1] is therefore not taken into account for simplicity reasons.

By summing up the irradiance values for the different colors, the resulting intensities detected by each face of the LAD have the same intrinsic error, due to the equal spectral responsivities of the diodes of each sensor board. By only considering the ratio between energy yields, and therefore between irradiance values, the resulting error is minimized.

3.1.1.2. Efficiency

The mono-facial panel addressed in this analysis has the same nominal efficiency of the front face of the bi-facial module, which is also equal to that of the back-side of the BFSP divided by the bi-faciality factor. The efficiency at any time however differs from the nominal efficiency, due to its dependence on the current, voltage, and temperature[26] within the cell. The changing position of the Sun, which regulates the intensity of incoming light, influences the current generated within the cell, while the voltage decreases with increasing temperature [21]. Maassen's analysis of the climate impact on the AMOLF solar panels shows that the efficiency of the reference HIT Si panel is only slightly affected by changes in cell's temperatures and solar irradiance values [17]. The largest divergence from the 19.4% nominal efficiency is observed at the beginning and end of sunny days [17], when the high incident angle of the prominent direct light effectively affects the absorptivity of the cell (Section 1.4). This analysis assumes a constant efficiency value, since significant efficiency variations occur when the energy yield of the solar cell is minimum.

Moreover, the solar irradiance considered in this chapter results from the sum of the values obtained by the different diodes of the LAD's faces (Section 3.1.1.1.). The quantum efficiency[27] of the solar cell is therefore erroneously assumed invariant of the photons' wavelength. However, the quantum efficiency of crystalline silicon is roughly constant over the visible and low infrared ranges [21]. By only considering the ratio of the energy yields and irradiance values, the error due to such assumption is minimized.

3.1.2. Irradiance ratio

Initially, all twelve sensor boards of the LAD were considered for the derivation of the bi-facial energy gain. The front six faces were analyzed in relation to the sky-facing side of a BFSP, while the sensor boards 7 to 12 were associated to its rear side.

[26] Due to their similar structure, the temperatures within a MF cell and a BF cell are assumed to be equal.
[27] The quantum efficiency is defined as the ratio between the number of minority carriers generated within the solar cell and the number of incident photons [21].

As in Section 2.5, the signal detected by each sensor board was assumed to be originated by a light-ray incident perpendicularly on the plane of the board. In order to associate the upper and lower hemispheres of the LAD to the front and rear sides of the BFSP, the intensity measured by each of the LAD's sensor boards was reduced by the projection of the respective face onto the horizontal[28] axis, according to Equations 3.1-2. The ratio of the total back (I_b) and front (I_f) intensities measured with all twelve sensor boards, according to Equations 3.3, was then compared to the ratio obtained by the single front and back faces (Equation 3.4) for a sunny and a cloudy day, as shown in Figure 3.2.

$$\alpha^{29} = 117° - 90° \qquad S = 1 + 5*\sin(\alpha) \qquad C = \sin(\alpha)/S \tag{3.1}$$

$$I_f = I_1*(1/S) + I_2*C + I_3*C + I_4*C + I_5*C + I_6*C$$
$$I_b = I_{12}*(1/S) + I_{11}*C + I_{10}*C + I_9*C + I_8*C + I_7*C \tag{3.2}$$

$$IRatio(b/f) = I_b / I_f \tag{3.3}$$

$$IRatio(12/1) = I_{12} / I_1 \tag{3.4}$$

In Equation 3.1, "S" represents the total projected surface of each hemisphere, "C" the contribution of each lateral face. The surface area of each face is not indicated in Equation 3.1, because it gets canceled out with the calculation of the ratio (Equation 3.3).

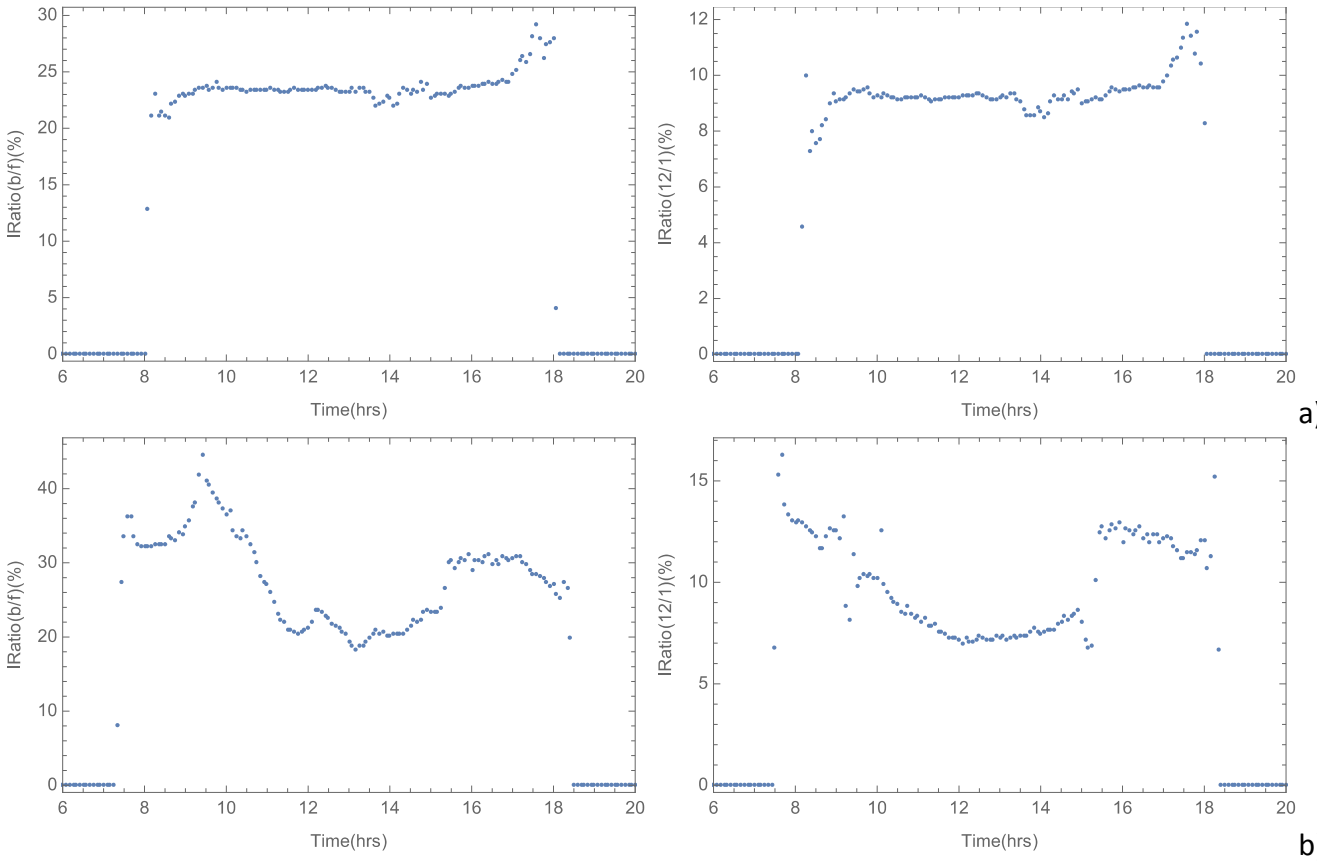

[28] The x-axis forms an angle with the ground which is equal to the tilt angle of the solar panels in the AMOLF solar field.
[29] Each face of the LAD forms an angle of approximately 117° with respect to the five adjacent faces.

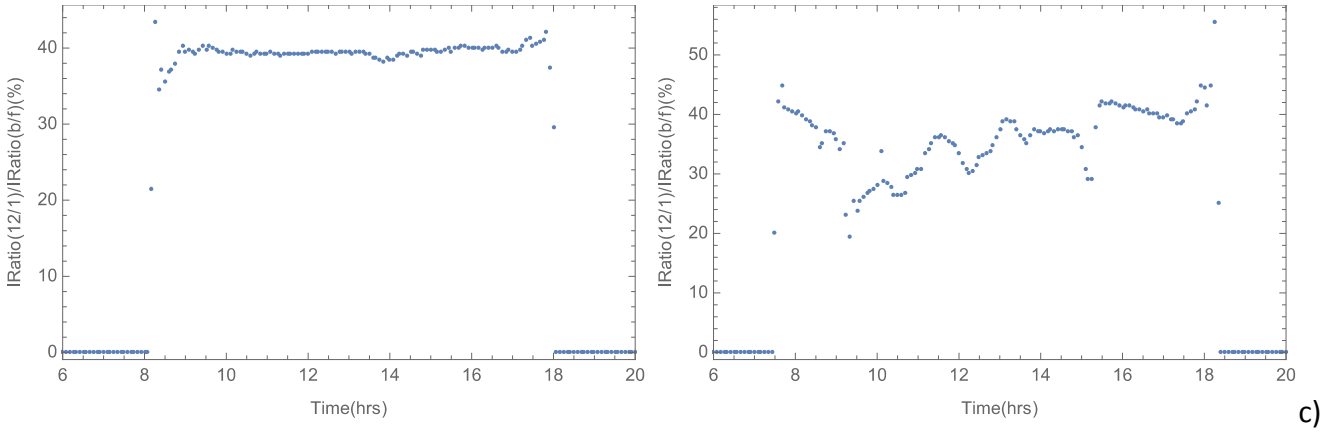

c)

Figure 3.2a,b,c: a,b) The graphs plot Equations 3.3 (left) and 3.4 (right) every 5 minutes, for a cloudy day (2nd of February 2019) (a) and for a sunny day (18th of February 2019) (b). c) The graphs plot the ratios of Equations 3.3 and 3.4 every 5 minutes, for a cloudy day (2nd of February 2019) (left) and for a sunny day (18th of February 2019) (right).

As shown in Figure 3.2a,b, the irradiance ratios of the back and front sides obtained by the single faces 12 and 1 and by all the upper and lower faces are different. Even though the observed data with mostly direct light fluctuate more intensely than those on a day with high diffusivity, due to the changing position of the Sun, the observed pattern in Figure 3,2c suggests a direct proportionality between Equation 3.4 and Equation 3.3, averaged over daytime, with a proportionality constant of nearly 0.4.

The analysis of only the front (1) and back (12) faces is advanced in this chapter in relation to the two sides of a bi-facial solar panel, while the consideration of the lateral contributions is resumed in the discussion of the energy results. The irradiance detected by the two opposing sensor boards indeed approximately resembles the data that a BFSP would obtain, since, like the two faces of the panel, they both have a field of view of 180° and the same inclination. Moreover, the normalized responsivity and reflectivity losses of the opposing LAD's faces are the same (Sections 2.2.3. and 2.3.1.). The exclusion of additional systematic errors due to differences in absorptivity of the sensors sustains the comparison with the opposing faces of a BFSP. The quasi-symmetric glass-to-glass system of a BFSP indeed guarantees a similar absorptivity for both sides; the bi-faciality factor only influences the detected solar power and not the incoming irradiance.

3.2. Results

Resulting from Equation 3.1 is a list of bi-facial energy gains every 5 minutes, for a given day. Figure 3.3 shows the energy gains that a BFSP with the same setting as the LAD's, would have obtained on two sunny and cloudy days.

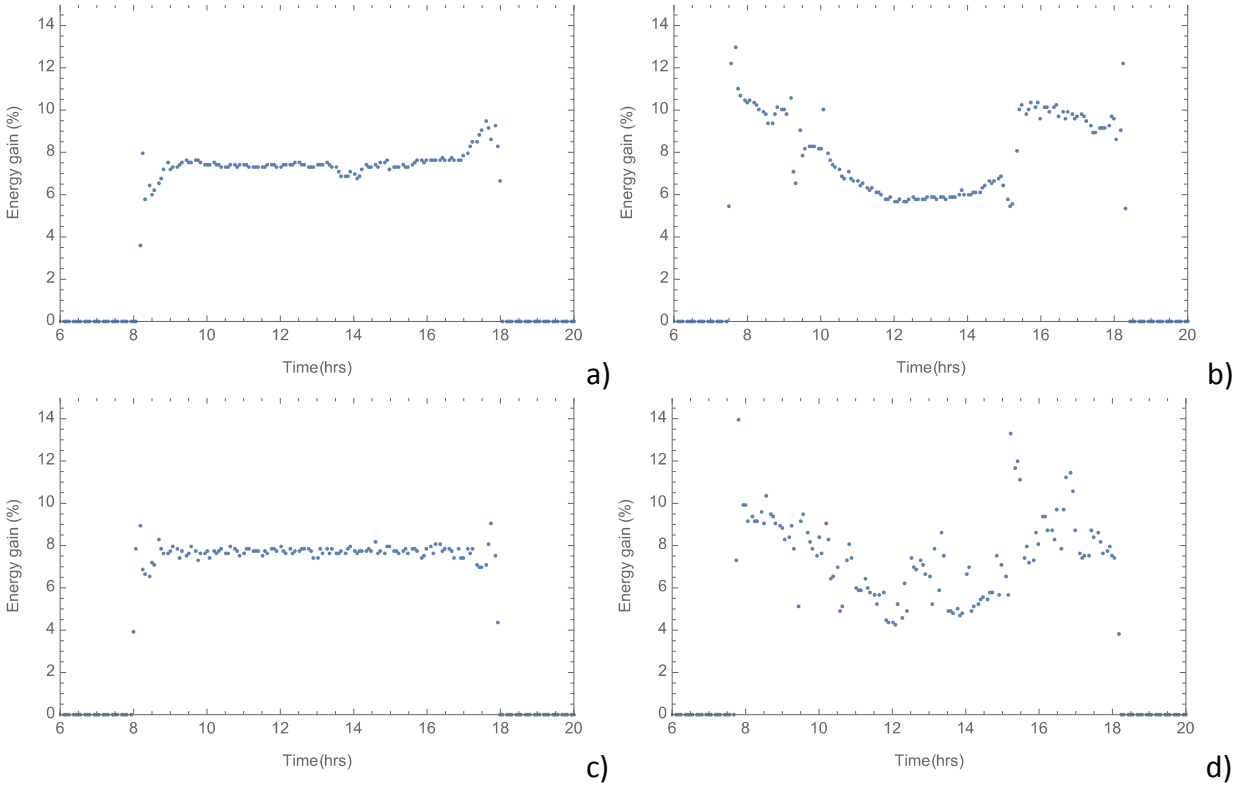

Figure 3.3a,b,c,d: The bi-facial energy gain is plotted over time for four different days. a) 2nd of February 2019 (cloudy); b) 18th of February 2019 (sunny); c) 5th of February 2019 (cloudy); d) 11th of February 2019 (sunny).

The energy gain, as shown in Figure 3.3, varies over time. The difference in divergences between a sunny day, Figure 3.3b,d, and a cloudy day, Figure 3.3a,c, is clear and follows from the prevalence of direct or diffuse light throughout the day. On a sunny day, the changing position of the Sun influences the energy generated by the back side of a BFSP. At early and late times, the high incident angles of the direct solar irradiance increase the photons' reflectance and scattering probabilities, therefore enhancing the reception probability of the rear face of the BFSP with respect to the central times of the day, when direct sunlight concentrates on the front face of the panel. On a cloudy day, diffuse light prevails and there is no leading direction in incident light: the observed bi-faciality gain is therefore roughly constant over time. The mean values of the energy gains (BG), of each day plotted in Figure 3.3, is contained in the interval [7.1;7.7]%.

By considering the energy outputs of the AMOLF mono-facial reference panel as a weight for the corresponding bi-facial gains, a more accurate estimate of the BG achieved on a given day is obtained. The weighted summation (Equation 3.2) relating the energy yields of BFPSs to those of MFSPs constrains the estimatitation of the BGs, for the previous four days, between 6.1 and 7.3%.

$$\frac{\sum_i^{288} BG(i) * Ymono(i)}{\sum_i^{288} Ymono(i)} \qquad (3.5)$$

The summations in Equation 3.2 go from 1 to 288, which is the number of data detections, for the bi-facial energy gains and mono-facial electric power outputs, throughout a day. The power outputs and

gains are indeed obtained every 5 minutes and are assumed constant for the 300 seconds preceding a detection, hence justifying the use of electric power outputs instead of the energy yields in Equation 3.2, due to the comnmon 300 multiplicative factor in the numerator and denominator.

3.2.1. Bi-facial energy gain: time-dependence

The bi-facial energy gain is proportional to the energy yields of mono-facial modules and inversely proportional to those of bi-facial modules. The energy outputs, as indicated in Section 3.1.1., depend on a series of time-dependent parameters, in particular on the direction of solar irradiance and on the cell's temperature. These parameters fluctuate throughout a day and even more throughout a year. In particular, towards the summer, the elevation angle[30] of the Sun increases and the cell's temperatures tend to be higher, while the opposite occurs towards winter. The position of the Sun and the temperature of the solar panel influence its efficiency, which influences the electric energy yields and bi-facial gains.

Analyzing the time relation between energy yields and bi-facial gains is a fundamental step towards the advancement of the accurate energy comparison between BFSPs and MFSPs. However, the few months' worth of data that supports the energy analysis of this thesis limits the accuracy of the estimation of the bi-facial energy gain throughout a year.

3.2.1.1. Electric energy output over a year

The relation between bi-facial energy gains and daily electric mono-facial energy outputs, developed for the available data of January, February, and March 2019, provides a significant basis to the derivation of the energy gains that a BFSP would experience throughout any given day of the year. By selecting a few representative sunny and cloudy days for the first months of 2019 and analyzing the energy gains corresponding to these days, a function that associates a BG value to a kilowatt-hours value is derived. Figure 3.4 shows the relation between BGs and the days' mono-facial energy outputs[31]; a fitting linear function of the data has been developed (Equation 3.6), which returns the bi-facial energy gain, given the mono-facial energy output in kWh:

$$BG = 7.68739 - (0.519474 * Y_{mono}) \quad (3.6)$$

[30] The height of the Sun measured from the horizontal [21].

[31] The energy outputs correspond to the power outputs of the AMOLF HIT Si panel multiplied by 300 seconds; the power output of the cell is indeed assumed constant for the 5 minutes period between each measurement. The AMOLF panel does not send a signal to the AMOLF storage with the power output value if the incident irradiance is lower than 50 W/m^2. The energy output per day is therefore given by the sum of the energy yields superior to a certain value determined by the irradiance limit.

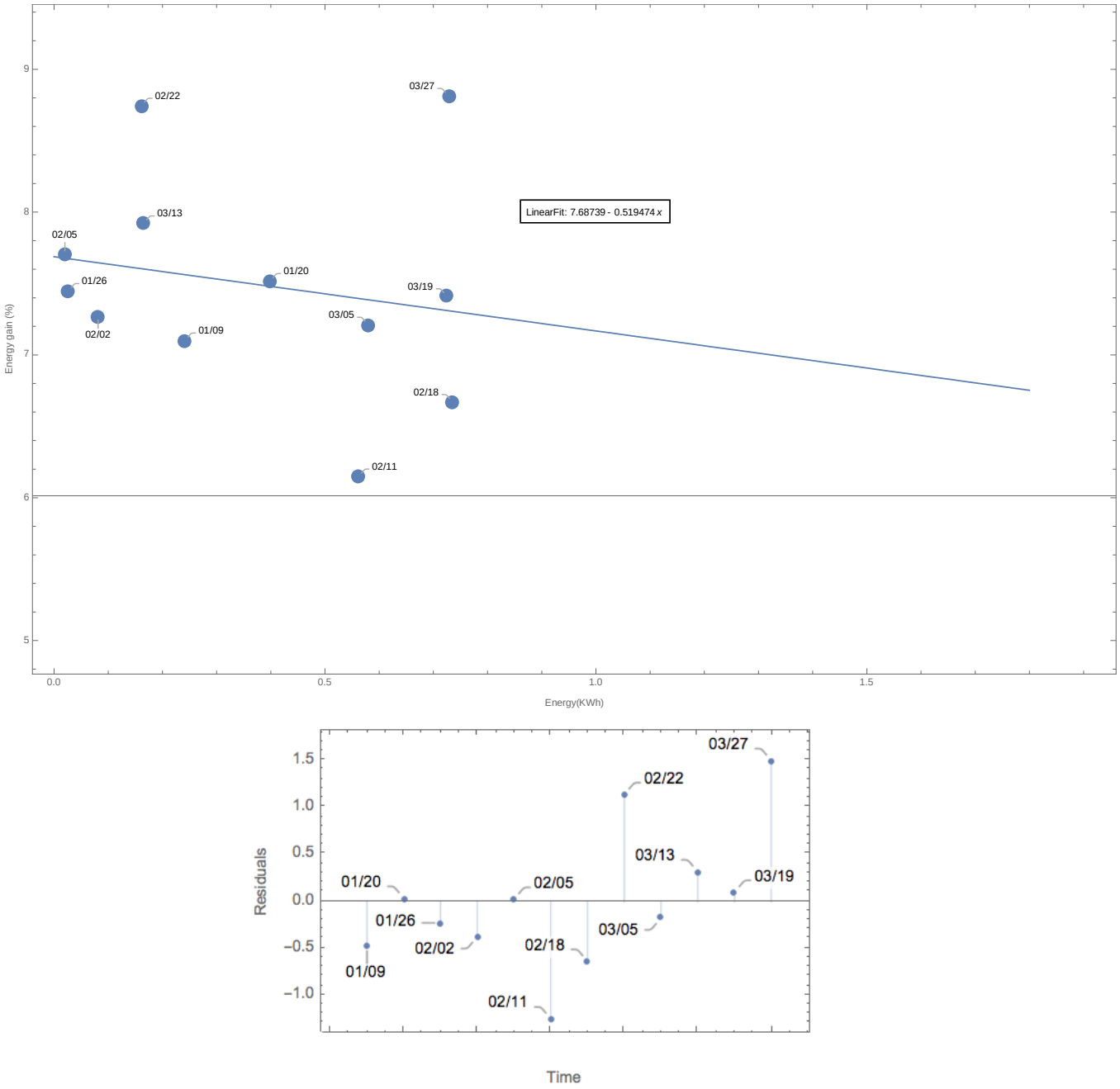

Figure 3.4: The plot shows the relation between bi-facial energy gain and energy output of a mono-facial solar cell. A fitting linear function has been developed to clarify the results. The data obtained on 4 sunny and 4 cloudy days do not perfectly fit to the relation BG = 7.68739 - 0.519474*(kWh) and the residuals are plotted on the bottom. The standard deviation given by the residuals to Equation 3.6 is 0.743128. The chosen dates (month/day) are indicated in the figure.

Figure 3.4 shows the inverse relation between energy gain and electric energy output. Such relation suggests that the minima of the BGs should be observed when the energy yields are maxima, for example towards summer.

By deriving a function of the energy yields per day for a previous year and comparing it with the energy yields, per day, obtained for the first months of 2019, one can estimate the BGs for the entire year. Figure 3.5 shows the time evolution of the energy output by selecting some representative days throughout 2018 and the first three months of 2019.

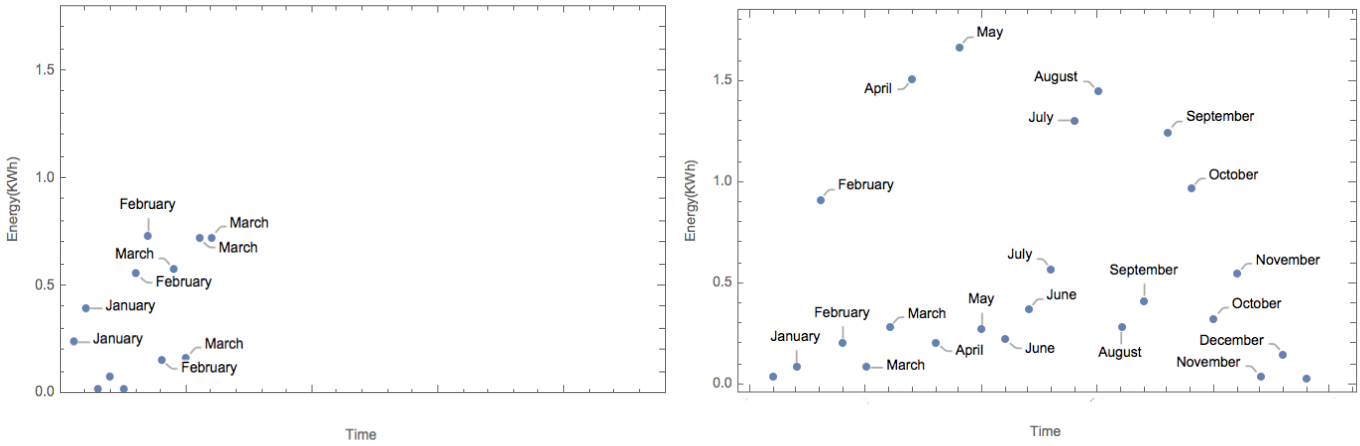

Figure 3.5a,b: The images show the relation between energy yields per day and time, over a period of one year. The image on the left (a) derives from the data obtained on twelve days between January and March 2019; the graph on the right (b) has been developed according to the energy outputs of the AMOLF HIT Si in 2018. Twenty-four random days were chosen for sampling the year 2018, equally divided into sunny and cloudy days.

Even though the energy outputs of the first months of 2019 seem generally higher than those of the chosen days in the first months of 2018, Figure 3.5 shows the predicted energy values for the following months. An increase in energy yields is expected towards the summer, with outputs exceeding 1kWh, while lower values should be observed throughout the rest of the year.

The energy yields for most days of the year should not exceed the maximum values obtained in March 2019. The empirical relation between bi-facial energy gain and mono-facial energy yield developed in Figure 3.4 is therefore expected to be accurate for the derivation of BGs for a whole year, even if higher uncertainty corresponds to the expected BG values for the summer season.

By manipulating Equation 3.5, the estimate of the bi-facial energy gain for a whole year is achieved: the summations over the data detections of a single day are replaced by summations from i=1 to i=24, the number of days shown in Figure 3.5b. The bi-facial gains for these days were calculated according to Equation 3.6 and the days' mono-facial energy outputs. The expected bi-facial energy gain resulting from the weighted summation over a whole year is about 7.15%.

3.3. Discussion

The energy gains obtained in Section 3.2. were derived through the consideration of only the front and back faces of the LAD. The contribution of the lateral sensors of the LAD to the calculation of the detected irradiance was estimated, for two different days, to measure an enhanced intensity ratio of about 150% with respect to the value derived from Equation 3.4 (Section 3.1.2.). The values obtained by considering the contributions of the lateral sensors are about 2.5 times higher than the irradiance ratios obtained by the single back and front faces, since the lower hemisphere and in particular the lower 5 lateral faces, detect relatively more light than the single face 12. By assuming a constant, time independent, proportionality factor of 2.5 relating Equations 3.3 and 3.4, and multiplying it by the expected bi-facial energy gain, averaged over a whole year, obtained at the end of last paragraph, the predicted bi-facial gain would be about 17.8%, a value much larger than 7.15%.

The analysis of bi-facial gains by Sun et al. [30] evaluated the average energy gains of bi-facial modules in Europe between 5 and 30%, with the lower value corresponding to an albedo value of 0.25 and a module height of 0m, and the higher value to an albedo higher than 0.5 and a module height of 1m. Even if the LAD's height is about 1m, the uncertainties concerning the albedo of the surface behind the instrument, limit the evaluation of the best intensity ratio value to be used for the energy analysis.

The cost-efficiency analysis advanced in this paper is based on the energy results obtained in Section 3.2.; the method based on the intensity ratio of only the back and front faces is preferred for simplicity reasons. The investigation of the measurements obtained by only two sensor boards indeed greatly reduced the running time of the code for the derivation of the BG.

Further research on the albedo effect on the LAD's measurements will justify the choice of one of the methods used to calculate intensity ratios.

Chapter 4

Cost-efficiency Analysis

The energy analysis of bi-facial systems is inconsequential if the total expenditures associated with the acquisition and operation of bi-facial systems exceed those of mono-facial systems by an amount larger than the bi-facial energy gain. The investigation into the differences of present and future expenses of the two solar panels ensures the completion of the more suitable cost-efficiency analysis.

4.1. Methodology

The comparison between the costs of electricity generated by a MFSP and a BFSP requires the discounting of future expenditure and energy losses to the net present value. The derivation of the levelized cost of electricity (LCOE), for the two modules with a given lifetime l_S, follows from the method proposed by Rodriguez-Gallegos et al. [24].

The long-term consideration of energy outputs and costs involves the examination of the energy losses due to the solar cells' degradation in time and of the fluctuations in time of operational, maintenance, and warranty costs as well as those of interest rates.

This cost-efficiency analysis assumes equal energy losses per year for both modules. The glass-to-glass system, as opposed to the glass-to-blacksheet configuration of MFSPs, is expected to improve the long-term durability of BFSPs with respect to MFSPs and therefore reduce their energy losses [25]. However, at the time of writing, the small amount of available data on the time variation of the energy output of this emerging solar technology limits the accuracy of the energy losses' analysis.

4.1.1. The levelized cost of electricity

The LCOE is the net present value of the cost of electricity generated by a certain source during its life-time. The levelized cost of electricity is given by the ratio between the total cost of the PV system, C_{PV} [USD], and the sum, over its lifetime, of the total energy it produces in the year y, $E^{(y)}_{PV}$ [Wh], discounted at present value, with discount rate DR [24]:

$$LCOE = \frac{C_{\mathrm{PV}}}{\sum_{y=1}^{\ell_S} \frac{E_{\mathrm{PV}}^{(y)}}{(1+DR)^y}} \tag{4.1}$$

where $E_{PV}^{(y)} = (E_{PV}^{(0)} * I^{(y)})$ and "I" corresponds to the energy degradation losses in the year y, as compared to year (y-1). Therefore, the energy generated in the current year, $E_{PV}^{(0)}$, can be taken out of the summation in the denominator of Equation 4.1.

4.1.1.1. The levelized cost of electricity ratio

In this chapter, the ratio between the LCOE of bi-facial and mono-facial modules is investigated for simplicity. By dividing the two levelized costs of electricity, indeed, the summations of the equal energy losses factor for BFSPs and MFSPs, $I^{(y)}/(1+DR)^y$, are canceled out. A cost ratio and an energy ratio are thus defined:

$$(LCOE_{bi} / LCOE_{mono}) = (C_{bi}/C_{mono})*(E_{mono}/E_{bi}) \tag{4.2}$$

In equation 4.2, a value lower than 1 would identify the bi-facial module as more cost-efficient, while a value larger than 1 would suggest the propensity towards standard mono-facial modules.

4.1.2. Cost estimations

The total costs associated with a photovoltaic system, from the moment of its fabrication to that of its retirement, imply a bank loan has been obtained in order to cover a portion of the initial investment costs. The total costs (C_{PV}) are then defined by [24]:

$$C_{PV} = C_{Bank,int} + C_{Bank,amor} + C_{own} + C_{war} + C_{insu} + C_{OM} \quad (4.3)$$

where $C_{Bank,int}$ [USD] and $C_{Bank,amor}$ [USD] indicate the amounts the borrower needs to pay to the bank because of the interest and loan principal, respectively; $C_{own.}$ [USD] represents the initial investment cost that is not covered by the bank loan, C_{war} [USD] the warranty cost of the solar inverter, and C_{insu} [USD] the insurance costs of the PV system. The total operation and maintenance costs associated with the PV system are defined by C_{OM} [USD]. The costs associated with the transportation of materials and personnel is not included in this analysis [24].

4.1.2.1. Initial investment

The magnitude of the required bank loan and the amount the owner has to pay immediately depend on the initial investment cost, $C_{ini,inv}$ [USD]. This is proportional to the capacity of the solar panel, therefore to the nominal[32] power of the solar panel's front face, $P_{STC,f}$ [W_P]. The initial investment cost is indeed defined by Rodríguez-Gallegos et al. as [24]:

$$C_{ini,inv} = P_{STC,f} \cdot (c_{sp} + c_{ins} + c_{ivt}^{(0)}) \quad (4.4)$$

where the cost coefficients c_{sp} [USD/W_p], c_{ins} [USD/W_p], and $c^{(y)}_{ivt}$ [USD/W_p] correspond to the acquisition of the solar panel, to its installation, and to the acquisition of the solar inverter in the year y, respectively.

4.1.2.2. Bank loan

The obtainment of a bank loan, l_{Bank} [%], expressed as a percentage of the initial investment, requires the respect of future fixed obligations. The total loan payment that must be achieved after a fixed period of dt_{Bank} years, is amortized in yearly amounts. The amortization is determined in such a way that the pay-off is initially mostly directed towards the interest costs ($C_{Bank,int}$ [USD]), while, subsequently, it aims to reduce the initial loan amount, also known as loan principal ($C_{Bank,amor}$ [USD]). The yearly amount that must be paid to the bank is therefore given by the sum of the yearly repayments towards interest costs and loan principal. Rodríguez-Gallegos et al. show that the total amounts to be paid-off, after dt_{Bank} years, for the interest costs and loan principal are given by [24]:

$$C_{Bank,int} = \sum_{y=1}^{dt_{Bank}} \frac{C_{ini,inv} \cdot l_{Bank} \cdot IR_{Bank} \cdot ((1 + IR_{Bank})^{dt_{Bank}+1} - (1 + IR_{Bank})^{y})}{(1 + IR_{Bank}) \cdot ((1 + IR_{Bank})^{dt_{Bank}} - 1) \cdot (1 + DR)^{y}} \quad (4.5)$$

[32] The nominal power corresponds to the maximum power generated at Standard Test Conditions. The Watt unit is substituted by W_p (watt-peak), which uniquely highlights the STC maximum power output.

$$C_{\text{Bank,amor}} = \sum_{y=1}^{dt_{\text{Bank}}} \left[\frac{IR_{\text{Bank}} \cdot (C_{\text{ini,inv}} \cdot l_{\text{Bank}} \cdot (1 + IR_{\text{Bank}})^{dt_{\text{Bank}}})}{((1 + IR_{\text{Bank}})^{dt_{\text{Bank}}} - 1) \cdot (1 + DR)^{y}} \right] - C_{\text{Bank,int}} \quad (4.6)$$

where l_{Bank} [%] refers to the bank loan, IR_{Bank} [%] to the interest rate, and DR [%] to the discount rate.

4.1.2.3. Own initial payment

The bank loan does not cover all initial costs; a certain amount must be paid by the solar panel's buyer. Naturally, this corresponds to the remaining initial investment costs minus those covered by the bank loan [24]:

$$C_{\text{own}} = C_{\text{ini,inv}} \cdot (1 - l_{\text{Bank}}) \quad (4.7)$$

4.1.2.4. Warranty costs of the PV inverter

An important component of a solar system is the PV inverter. The conversion of PV generated direct current into alternating current is indeed fundamental for the production of solar electricity. Most inverters are protected by a guarantee, valid for a period of w_{ivt} years. This analysis, developed according to [24], assumes an initial warranty period that gets extended periodically. The costs of extending the warranty period are proportional to the costs of the inverter in that year y, $c^{(y)}_{\text{ivt}}$ [USD/W_p]. Rodríguez-Gallegos et al. calculated the total amount related to the warranty extensions over the lifetime of the solar cell to be [24]:

$$C_{\text{war}} = \sum_{i=1}^{\lfloor l_S / w_{\text{ivt}} \rfloor} P_{\text{STC,f}} \cdot c_{\text{ivt}}^{(i \cdot w_{\text{ivt}})} \cdot \pi_{\text{ivt}}^{(i \cdot w_{\text{ivt}})} \cdot \frac{(1 + IR)^{i \cdot w_{\text{ivt}}}}{(1 + DR)^{i \cdot w_{\text{ivt}}}} \quad (4.8)$$

where l_s/ w_{ivt} indicates the number of times the inverter's warranty must be extended, and $\pi_{\text{ivt}}^{(y)}$ [%] the fraction of the inverter cost in the year y that must be paid in order to renovate the guarantee, IR [%] the inflation rate. The i starts from 1 since the initial guarantee does not need to be renovated in the year 0 and $\pi_{\text{ivt}}^{(0)}$ would be 0; the summation limit therefore actually corresponds to (l_s/w_{ivt} – 1) if an initial guarantee is assumed.

4.1.2.5. Insurance costs

Alongside the inverter's guarantee, the owner of a PV system is insured against damages to it. The yearly amount corresponding to the coverage of a solar module is proportional to the initial investment costs and therefore to the capacity of the panel itself. Rodríguez-Gallegos et al. derived the following formula for the total insurance costs over the lifetime of the solar system [24]:

$$C_{\text{insu}} = \sum_{y=1}^{\ell_S} C_{\text{ini,inv}} \cdot c_{\text{insu}} \cdot \frac{(1+IR)^y}{(1+DR)^y} \tag{4.9}$$

where c_{insu} [%] is the proportionality factor connected to the initial investment costs.

4.1.2.6. Operation and Maintenance costs

Finally, the last costs to account for, after the acquisition of a solar module, are related to the operation and maintenance of the PV system. Mechanical and optical issues are frequent, especially in locations affected by sharp fluctuations in weather conditions, and maintenance is required every year. These costs, as the insurance costs, are proportional, according to a given coefficient c_{OM} [USD/year/W_p], to the capacity of the solar panel; for a single panel, such expenditures are minimal. Rodríguez-Gallegos et al. estimate them at [24]:

$$C_{\text{OM}} = \sum_{y=1}^{\ell_S} P_{\text{STC,f}} \cdot c_{\text{OM}} \cdot \frac{(1+IR)^y}{(1+DR)^y} \tag{4.10}$$

4.2. Results

4.2.1. Cost estimations

Cost parameters for MFSPs and BFSPs are derived from the data concerning the Netherlands contained in the research by Rodríguez-Gallegos et al. [24]. The values assumed in this analysis were valid, in 2018, for a location with a latitude of 51.971 and a longitude of 4.927 [21], while Amsterdam's coordinates are: 52.3680° N, 4.9036° E. The discrepancy between the two locations is expected to cause a minimal inaccuracy in the results. The lifetime of both modules is assumed to be 25 years, while the capacity of their front faces, $P_{STC,f}$, 1MW_p [24].

The costs related to bi-facial systems are in certain cases higher than those concerning standard mono-facial systems. The installation, operation and maintenance (O&M) costs are estimated to be 0.92% higher for BFSPs than those for MFSPs, since a larger PV active area correspond to the former; the installation and O&M costs contribute to only 0.8% of the total cost per watt-peak. The inverter costs are assumed to be 20% higher for BFSPs than for MFSPs, since Rodríguez-Gallegos et al. indicate the need to increase the capacity of bi-facial solar inverters by at least 20% with respect to those for MFSPs; a linear relation between inverter's capacity and costs is assumed. The costs associated with the acquisition of the inverter contribute to about 7% of the total costs of a solar system [11] which cause the total costs of BFSPs to be about 0.02 USD/W_p higher than those of MFSPs. The fabrication costs of a solar module represent about 20% of the total costs associated to the system [11]. Fabrication costs are therefore responsible for about 0.035 USD/W_p out of the total difference between the costs per watt-

peak between BFSPs and MFSPs. The differences between insurance and inverter's warranty costs of the two solar systems are responsible for additional cost disparities between BFSPs and MFSPs.

The inflation (IR) and discount (DR) rates account for the calculation of the net present value of a future asset; they are time-dependent, but Rodríguez-Gallegos et al. assume they have a constant value, due to the limited available data to forecast their values in the future [24].

The results for the total costs of a solar module, per unit of watt-peak, $C_{PV,Wp}$ [USD/W_p], are given in table 4.1 [24]:

	MFSP	*BFSP*
$C_{PV,Wp}$ *[USD/W_p]*	**1.34**	**1.43**

Table 4.1: The table shows the total cost per unit of W_p of mono-facial and bi-facial modules in the Netherlands [24].

4.2.1.1. Cost ratio

The cost ratio between the total costs of bi-facial solar panels and mono-facial modules is therefore given by:

$$C_{bi}/C_{mono} = 1.067 \tag{4.11}$$

The consideration of the ratio between the LCOEs, rather than the actual single values, limit the dependence of the result of Equation 4.11 on the assumptions made by Rodríguez-Gallegos et al. during their analysis [24].

The values included in Table 4.1 derive from the calculations of the total costs of solar systems with an installed capacity of 1 MW_p. The total costs are directly proportional to $P_{STC,f}$ and the cost parameters are scaled to a capacity of 1 MW_p in the same way for both MFSPs and BFSPs. By assuming such a high capacity, all prices are scaled according to the principle of economy of scale. Lower costs per unit of watt-peak are obtained by the analysis of Rodríguez-Gallegos et al. [24] with respect to the costs predicted the International Renewable Energy Agency [11]. A difference of more than 1 USD corresponds to the predicted total expenditures of MFSPs per W_p, with current price estimations, obtained by considering a single standard module [11] and an installed capacity of 1 MW_p [24]. By taking the ratio of the values in Table 4.1, the error due to the reduced expenses resulting from increasing the number of solar units, is reduced, since the same assumptions are considered for MFSPs and BFSPs. The cost analysis is, therefore, relevant to the cost-efficiency analysis developed in this paper, even though the energy results of Chapter 3 were derived according to the power output of the AMOLF monocrystalline heterojunction silicon solar panel (HIT Si), which has a maximum capacity of 245 Wp.

4.2.2. Energy estimations

The energy analysis concluded in Chapter 4 indicates a bi-facial energy gain, averaged over a year, of about 7.15%. Since this analysis assumes equal energy-degradation over time for the two modules, the energy ratio is thus defined as:

$$E_{mono}/E_{bi} = 0.933 \quad (4.12)$$

4.2.3. The levelized cost of electricity ratio

The cost-efficiency analysis of bi-facial and mono-facial panels concludes that the best module to be installed at AMOLF is a bi-facial system. The ratio of the levelized costs of electricity of the two solar panels derived in this thesis (Equation 4.2) is indeed 0.995. A 0.5% lower LCOE value is therefore associated with BF systems with respect to their mono-facial counterparts.

The 0.995 differs from the ratio of $LCOE_{bi}$ and $LCOE_{mono}$ obtained by Rodríguez-Gallegos et al., 0.981, by only 1.4% [24]. Rodríguez-Gallegos et al calculated the average energy production per day, per unit of watt-peak, discounted over the lifetime of the cell, to be 2.96Wh for BFSPs and 2.73Wh for MFSPs, in the Netherlands [24]. The ratio of these energy values would suggest the assumption of an average bi-facial energy gain of about 8.4%. The higher BG value considered in [24] with respect to the 7.15% assumed here is partly responsible for the observed 1.4% disparity between the results of the LCOEs' ratio achieved in this thesis and in the analysis by Rodríguez-Gallegos et al. [24]. Furthermore, the simplified assumption of equal energy degradation of BFSPs and MFSPs is also responsible for the discrepancy between the final results of this thesis and of the analysis by Rodríguez-Gallegos et al.

The proximity of the results obtained in this thesis and in [24] supports the choice of the method advanced in this thesis for the energy analysis, which is based on the derivation of the irradiance ratio between the back face and the front face of the LAD.

Chapter 5

Conclusion and discussion

The transition of the energy supply sector towards sustainable energy sources requires the employment at a large scale of renewable energies, and of solar technologies in particular. This thesis advances an accessible method to evaluate the most-coefficient photovoltaic model for a specific location. The analysis developed in this paper is specific to the installation of a solar module in the solar

field of the FOM institute AMOLF, in Amsterdam, Netherlands, but a similar method could be employed in other locations. The result of the cost-efficiency analysis identifies the bi-facial solar panel as a better alternative with respect to the standard mono-facial module in the AMOLF solar field.

The methodology of this cost-efficiency analysis follows from the derivation of the ratio between the levelized costs of electricity (LCOE) of BFSPs and MFSPs. The AMOLF light ambiance detector (LAD) provides the empirical background to the energy analysis, while the investigation of the total costs associated with the two solar modules is developed according to the cost-efficiency analysis of BFSPs and MFSPs by Rodríguez-Gallegos et al. [24].

In Chapter 2, the specifics and functionalities of the LAD are presented. The detector provides information on direct and indirect light by measuring the incoming solar irradiance through twelve sensor boards disposed in a dodecahedral geometry, for the blue, green, red, and infrared ranges of the electromagnetic spectrum. The data obtained for a specific day are suitable to the inference of the portion of diffuse and reflected light incident on the LAD and of the ideal orientation of a solar panel throughout that day. The calibration of the light and temperature sensors of the instrument, prior to the installation of the LAD in the AMOLF solar field, suggests a significant level of inaccuracy of the conversion functions, which convert the LAD's raw output into irradiance values expressed in W/m^2. The measurement errors during the calibration process and the assumption of a linear relation between raw data and actual intensity values are responsible for a conversion precision lower than 70% when the incoming irradiance falls below $140W/m^2$.

In Chapter 3, the energy analysis is advanced. This is based on the calculation of the energy gain that a BFSP would achieve in the AMOLF solar field and is thus based on the estimation of the ratio of the incoming irradiance that the back side and front side of the panel would detect. The method advanced in this thesis considers the ratio of the intensity values obtained by only the back and front faces of the LAD, for the association with the intensity ratio of the back and front sides of a BFSP, rather than the ratio of irradiance values obtained by the six upper and six lower faces of the LAD. The estimation of the energy gain that a BFSP would achieve throughout a whole year was derived according to the evaluation of the BGs for the available data of a few representative days of 2019 and the development of a linear function relating energy gains and energy outputs of the AMOLF mono-facial silicon solar panel (HIT Si). By considering the energy yields of the HIT Si module on a few representative days of 2018, by comparing them to the energy yields of the previously selected days of 2019, and by applying the linear function relating BGs and mono-facial energy outputs, the energy gain that a BFSP would obtain throughout a year at AMOLF was predicted to be 7.15%.

In Chapter 4, the cost analysis of bi-facial and mono-facial modules is developed according to the methodology adopted by Rodríguez-Gallegos et al. [24]. The evaluation of the total costs associated to the two solar systems assumes that a bank loan has been obtained to cover part of the initial costs, that the warranty of the solar inverter is extended periodically, and that the panels are covered by insurance. The assumption of an installed solar capacity of 1 MW_p by Rodríguez-Gallegos et al. render the total costs, per unit of watt-peak, associated to BFSPs and MFSPs lower than what would have been achieved by only considering single modules. However, the consideration of the ratio between the cost estimations limits the dependence of the obtained 1.067 value on the assumptions made by Rodríguez-Gallegos et al.

The levelized cost of electricity of a bi-facial solar system installed at AMOLF was calculated to be 0.5% lower than that of its mono-facial counterpart. The proximity of this result with the value obtained by Rodríguez-Gallegos et al. increases the credibility of the cost-efficiency analyses advanced in this paper and in [24]. Moreover, the small discrepancy between the results of this analysis and [24] supports the choice of the intensity ratios based on the consideration of only the back and front faces of the LAD and increases the confidence on the conversion functions developed through the calibration of the LAD's sensors.

Bibliography

1. ams. 2017. TCS3400 Color Light-to-Digital Converter. ams. Premstaetten (AT): 1-34. Available from: https://ams.com/documents/20143/36005/TCS3400_DS000411_5-00.pdf/5e66e18f-b76c-3245-47a7-1813b423c846
2. Aspnes DE, Studna AA. 1983. Dielectric functions and optical parameters of Si, Ge, GaP, GaAs, GaSb, InP, InAs, and InSb from 1.5 to 6.0 eV. Phys. Rev. B. [Internet]. [cited 2019 May 13]; 27(2): 985-1009. Available from: https://journals.aps.org/prb/abstract/10.1103/PhysRevB.27.985 doi: 10.1103/PhysRevB.27.985
3. Beadie G, Brindza M, Flynn RA, Rosenberg A, Shirk JS. 2015. Refractive index measurements of poly(methyl methacrylate) (PMMA) from 0.4–1.6 µm. Appl. Opt. [Internet]. [cited 2019 May 14]; 54(31): F139-F143. Available from: https://www.osapublishing.org/ao/abstract.cfm?uri=ao-54-31-F139
4. Bellini E. 2019 Feb 20. Bifacial modules ridin' down the highway. [Internet]. PV Magazine. Available from: https://www.pv-magazine.com/2019/02/20/bifacial-modules-ridin-down-the-highway/
5. Bruckner T, Bashmakov IA, Mulugetta Y, Chum H, Navarro ADLV, Edmonds J, Faaij A, Fungtammasan B, Garg A, Hertwich E, et al. 2014 Energy Systems. In: Edenhofer O, Pichs-Madruga R, Sokona Y, Farahani E, Kadner S, Seyboth K, Adler A, Baum I, Brunner S, et al., editors. Climate Change 2014: Mitigation of Climate Change. Contribution of Working Group III to the Fifth Assessment Report of the Intergovernmental Panel on Climate Change. Cambridge (UK) and New York (NY): Cambridge University Press. p. 511-597.
6. Cuevas A. 2005. The early history of bifacial solar cells. In: 20TH, European photovoltaic solar energy conference; 2005; Barcelona, Spain. Munich (DE): WIP-Renewable Energies. P, 801-805.
7. [DNE] Dutch New Energy Research. 2019. Dutch Solar Trend Report 2019 [Internet]. Expo Haarlemmermeer: Vijfhuizen (NL): Solar Solutions Int. [cited 2019 May 1].
8. EKO. [date unknown]. MS-711 Spectroradiometer. Den Haag (NL): EKO Instruments Co. Available from: https://eko-eu.com/products/solar-energy/spectroradiometers/ms-711-spectroradiometer/pdf
9. Giancoli DC. 2013. Physics for Scientists & Engineers with Modern Physics. Fourth Edition. London (UK): Pearson. 1426 p.
10. Gielen D, Kempener R, Taylor M, Boshell F, Seleem A, 2016. Letting in the Light: How Solar Photovoltaics Will Revolutionise the Electricity System. Abu Dhabi (UAE): International Renewable Energy Agency (IRENA). Available from: https://www.res4africa.org/wp-content/uploads/2016/09/IRENA_Letting_in_the_Light_2016.pdf
11. [IRENA] International Renewable Energy Agency [Internet]. 2012. Renewable energy technologies: cost analysis series. Solar Photovoltaics. Abu Dhabi (UAE): International Renewable Energy Agency. (IRENA). Available from: https://www.irena.org/documentdownloads/publications/re_technologies_cost_analysis-solar_pv.pdf
12. Jäger K, Olindo I, Smets AHM, Swaaij VRACMM, Zeman M. 2014. A Little Hystory of Solar Cells. In: Jäger K, Olindo I, Smets AHM, Swaaij VRACMM, Zeman M. Solar Energy. Delft (NL): Delft University of Technology. p. 151-154.
13. Jenkins FA, White HE. 1957. Fundamentals of Optics. 3rd ed. New-York (NY): McGraw-Hill. p. 766

14. Kersten M. 2018. Outdoor solar cell performance [Bachelor thesis]. University of Amsterdam.
15. Malitson IH. 1965. Interspecimen Comparison of the Refractive Index of Fused Silica. Opt. Soc. Am. [Internet]. [cited 2019 May 14]; 55(10): 1205-1209. Available from: https://www.osapublishing.org/josa/abstract.cfm?uri=josa-55-10-1205
16. Marion B, MacAlpine S, Deline C, Asgharzadeh A, Toor F, Riley D, Stein J, Hansen C. 2017. A Practical Irradiance Model for Bifacial PV Modules. In: 2017 IEEE 44th Photovoltaic Specialist Conference (PVSC); 25-30 Jun 2017; Washington (DC). Piscataway (NJ): Institute of Electrical and Electronics Engineers (IEEE). p, 1537-1542. Available from: https://www.nrel.gov/docs/fy17osti/67847.pdf doi: 10.1109/PVSC.2017.8366263
17. Maassen T. 2017. The effect of light diffuseness on the outdoor performance of thin film solar cells [Bachelor thesis]. University of Amsterdam.
18. Nelson J. 2003. The physics of solar cells. 1st ed. London (UK): Imperial College Press. p. 384.
19. [NRC] National Research Council. 2015. Climate Intervention: Reflecting Sunlight to Cool Earth. [Internet]. Washington (DC): The National Academies Press; [cited 2019 May 6]. Available from: https://doi.org/10.17226/18988
20. [NREL] National Renewable Energy Laboratory [Internet]. 2018. Photovoltaic Research; [cited 2019 Apr 27]. Available from: https://www.nrel.gov/pv/perovskite-solar-cells.html
21. [PVE] Photovoltaic Education [Internet]. 2019. PV Education; [cited 2019 Mar 1]. Available from: https://www.pveducation.org/
22. Pujari NS, Cellere G, Falcon T, Hage F, Zwegers M, Bernreuter J, Haase J, Yakovlek S, Coletti G, Romijn I, et al. 2017. International technology roadmap for photovoltaic (ITRPV): 2017 results. 9th ed. ITRPV. Available from: https://pv.vdma.org/documents/105945/26776337/ITRPV%20Ninth%20Edition%202018%20including%20maturity%20report%2020180904_1536055215523.pdf/a907157c-a241-eec0-310d-fd76f1685b2a
23. Ritchie H, Roser M. c2019. Global primary energy consumption [Internet]. Our World in Data; [cited 2019 May 3]. Available from: https://ourworldindata.org/grapher/global-primary-energy
24. Rodríguez-Gallegos CD, Bieri M, Gandhi O, Singh JP, Reindl T, Panda SK. 2018. Monofacial vs bifacial Si-based PV modules: Which one is more cost-effective? SEJ. [Internet]. [cited 2019 Apr 28]; 176: 412-438. Available from: https://www.sciencedirect.com/science/article/pii/S0038092X18309915
25. Romijn I. [date unknown]. Bifacial PV – now and in the future [Internet]. ECN: Petten (NL). Available from: http://sundaynl.nl/u/files/a2%20ingrid%20romijn.pdf
26. Rycroft M. 2018 May 9. Bifacial solar PV modules give increased power output potential. [Internet]. Energize. Available from: https://www.ee.co.za/article/bifacial-solar-pv-modules-give-increased-power-output-potential.html
27. Vasseur V, Kemp R. 2014. The adoption of PV in the Netherlands: A statistical analysis of adoption factors. RENEW SUST ENERG REV. [Internet]. [cited 2019 May 1]; 41: 483-494. Available from: https://www.sciencedirect.com/science/article/pii/S1364032114006960
28. Siyu g, Walsh TM, Peters M. 2013. Vertically mounted bifacial photovoltaic modules: A global analysis. Energy. [Internet]. [cited 2019 May 30]; 61: 447-454. Available from: https://www.sciencedirect.com/science/article/abs/pii/S0360544213007275
29. Spectrum of Solar Radiation (Earth) [Internet]. Wikimedia Commons; c2013 [updated 2019 Feb 25; cited 2019 May 7]. Available from: https://commons.wikimedia.org/wiki/File:Solar_spectrum_en.svg

30. Sun X, Khan MR, Deline C, Alama MA. 2018. Optimization and performance of bifacial solar modules: A global perspective. APPL ENERG. [Internet]. [cited 2019 May 24]; 212: 1601-1610. Available from: https://www-sciencedirect-com.proxy.uba.uva.nl:2443/science/article/pii/S0306261917317567

Code

The Energy analysis was conducted through the use of the coding program Mathematica. The program should be run in Mathematica version 13.3. The code is available for download at: https://drive.google.com/file/d/19hzmchRweyAL21V1ZRabb0h0IU7K2AO0/view?usp=sharing